



Title	Superconductivity of hydrogen-rich metal hydride Li <sub>5</sub> MoH <sub>11</sub> under high pressure
Author(s)	Dezhong, Meng
Citation	大阪大学, 2018, 博士論文
Version Type	VoR
URL	<a href="https://doi.org/10.18910/70772">https://doi.org/10.18910/70772</a>
rights	
Note	

*The University of Osaka Institutional Knowledge Archive : OUKA*

<https://ir.library.osaka-u.ac.jp/>

The University of Osaka

# **Superconductivity of hydrogen-rich metal hydride $\text{Li}_5\text{MoH}_{11}$ under high pressure**

DEZHONG MENG

SEPTEMBER 2018

# **Superconductivity of hydrogen-rich metal hydride $\text{Li}_5\text{MoH}_{11}$ under high pressure**

A dissertation submitted to  
**THE GRADUATE SCHOOL OF ENGINEERING SCIENCE  
OSAKA UNIVERSITY**

in partial fulfillment of the requirements for the degree of  
**DOCTOR OF PHILOSOPHY IN ENGINEERING**

**BY**

**DEZHONG MENG**

**SEPTEMBER 2018**

# Abstract

Hydrogen was predicted to show metallic behavior and even a possible high-temperature superconductor under sufficient pressurization [1]. Further calculations predicted that pure hydrogen showed atomic phase under  $> 500$  GPa and became a superconductor with the transition temperature ( $T_c$ ) of 300-350 K [2]. While the high pressure is beyond the present experimental conditions, it is predicted that some hydrogen-rich compounds could be metallic and superconductive under comparable lower pressure than that of pure hydrogen due to the chemically pre-compressed from relative heavier elements [3]. In fact, sulfur hydride ( $H_2S$ ), one of the hydrogen-rich compounds was recently reported to be a superconductor with a high  $T_c$  of 203 K under 150 GPa [4], which strongly motivates the superconductor research in hydrogen-rich compounds.

Transition metals could combine with hydrogen atoms to form the close-packed structures with a signally rich variety of hydrogen coordination modes. One of the hydrogen-rich metal hydride  $BaReH_9$  with 9 hydrogen atoms in the unit cell showed superconductivity at a pressure above 100 GPa with a maximum  $T_c$  near 7 K [5]. Here we focused on  $Li_5MoH_{11}$  which is one of the hydrogen-rich metal hydrides with 11 hydrogen atoms in the unit cell. According to the calculation of the density of states, the valence band of  $Li_5MoH_{11}$  is dominated by the hydrogen  $1s$  orbital and the band gap is 4 eV at ambient pressure [6]. Therefore,  $Li_5MoH_{11}$  can be expected to show the metallization and possible higher  $T_c$  superconductivity, whose character comes from hydrogen. The electrical resistance and the crystal structure of  $Li_5MoH_{11}$  were investigated extensively under high pressure and low temperature.

The  $Li_5MoH_{11}$  sample was synthesized by high-pressure and high-temperature treatments and provided by Prof. Orimo in Tohoku University. The sample was an insulator at ambient pressure and exhibited insulating behavior up to 84 GPa. The insulating behavior was suppressed by the increasing of pressure. The superconducting behavior with a small resistance reduction at low temperature was found at pressure around 100 GPa, which was confirmed by the applying of magnetic field. Intriguingly the appearance of the superconductivity of  $Li_5MoH_{11}$  displayed an effect of annealing time dependence, which

was also observed in the previous reports in BaReH<sub>9</sub> [5]. The onset  $T_c$  of the Li<sub>5</sub>MoH<sub>11</sub> sample presented 5.4 K at 100 GPa and exhibited a negative pressure dependence showing the decrease to 4.5 K at 155 GPa. By further increasing the pressure,  $T_c$  rapidly increased to 6.4 K at 160 GPa and remained almost unchanged until 210 GPa the highest pressure of this experiment. Synchrotron powder X-ray diffraction measurements results revealed that Li<sub>5</sub>MoH<sub>11</sub> demonstrates no structural phase transition up to 130 GPa keeping with the hexagonal structure, which claims that the observed superconducting signal is not from high-pressure by-product but from Li<sub>5</sub>MoH<sub>11</sub>.

These results highlight the important role of pressure in exploring the superconductivity of hydrogen-rich hydrides, which promote future high-pressure experiments for the nature of dense pure hydrogen with metallic state and the possible high-temperature superconducting behavior. Furthermore, the study of hydrogen-rich hydride provides the insight into the new superconducting phase at ambient pressure for the extensive utilization in electronic materials and hydrogen storage materials.

## Document structure

This document consists of four chapters. Each chapter is further divided into sections and subsections. Chapter 1 gives a description of the introduction and background for this work. Chapter 2 illustrates the experimental detail. The experimental results and discussions are given in Chapter 3. Furthermore, the conclusions together with some perspectives for future work are presented in Chapter 4.

## Reference

- [1] N.W. Ashcroft, Phys. Rev. Lett. **21**, 1748 (1968).
- [2] J.M. McMahon, *et al.*, Rev. Mod. Phys. **84**, 1607 (2012).
- [3] N.W. Ashcroft, Phys. Rev. Lett. **92**, 187002 (2004).
- [4] A.P. Drozdov, *et al.*, Nature **525**, 73 (2015).
- [5] T. Muramatsu, *et al.*, J. Phys. Chem. C **119**, 18007 (2015).
- [6] S. Takagi, *et al.*, Sci. Rep. **7**, 44253 (2017).

# Contents

Chapter 1. Introduction .....	1
1.1 High pressure science .....	1
1.2 Superconductivity .....	3
1.2.1 The history of superconductivity .....	3
1.2.2 BCS theory.....	5
1.3 Superconductivity under pressure.....	7
1.4 Superconductivity of hydrogen and hydrides .....	9
Chapter 2. Experimental methods .....	24
2.1 Diamond anvil cell (DAC).....	24
2.2 Preparation for DAC .....	32
2.3 Sample preparation .....	39
2.4 Pressure determination.....	41
2.5 High pressure measurements of DACs.....	42
Chapter 3. Superconductivity of $\text{Li}_5\text{MoH}_{11}$ under high pressure .....	48
3.1 Introduction of $\text{Li}_5\text{MoH}_{11}$ .....	48
3.2 The result of long time annealing .....	50
3.2.1 The temperature dependence of electrical resistance under pressure .....	51
3.2.2 The effect of magnetic field on the temperature dependence of resistance.....	59
3.2.3 The diagram of pressure versus temperature .....	61
3.3 Results of short time annealing.....	62
3.3.1 The temperature dependence of electrical resistance under pressure .....	63

3.3.2 The effect of magnetic field on the temperature dependence of resistance.....	66
3.3.3 The diagram of pressure versus temperature .....	68
3.4 The synchrotron powder XRD under high pressure .....	69
3.5 Discussion.....	71
3.5.1 The time dependence behavior .....	71
3.5.2 The superconductivity of $\text{Li}_5\text{MoH}_{11}$ .....	73
3.5.3 The phase diagram of $\text{Li}_5\text{MoH}_{11}$ .....	74
3.5.4 The comparison of $\text{Li}_5\text{MoH}_{11}$ and $\text{BaReH}_9$ .....	76
Chapter 4. Conclusions .....	81
Published works .....	83
Acknowledgements .....	84

# Chapter 1. Introduction

In this chapter, the development of high pressure science and its effect on matter, the history of superconductivity and BCS theory, the theory of superconductivity under pressure and the superconductivity of hydrides under high pressure will be presented.

## 1.1 High pressure science

Pressure, temperature and chemical composition are three essential thermodynamics factors of the state of matter. Our daily lives experience the influence of pressure. The ambient pressure at sea level on earth is equal to 101,325 Pa, which is approximately one atmosphere. While the pressure of earth inner core is about 360 GPa [1]. The pressure in nature can extend over a quite large range from  $10^{-22}$  Pa in the intergalactic space to  $10^{35}$  Pa in the center of the neutron star.

The study of high pressure science mainly focused on gaseous and liquid state at the beginning stage. The early development of pressure reported was the investigation of water by John Canton in 1762 [2]. While the pressure range was restricted at that time owing to the high-pressure apparatus. In 1880s, a hydraulic manometer which could bring the pressure above 300 MPa was designed by a French scientist E. Amagat [3]. The high-pressure science entered into a rapid development era by the contribution of P.W. Bridgman. A set of opposing anvils was designed to generate high pressure exceeding 10 GPa, which called the Bridgman anvil later [4-6]. Due to his pioneering work in the field of high pressure science field, P.W. Bridgman was honored the Nobel Prize of physics in 1946. In 1950s, the hardest material in nature diamond was used for the engendering of high pressure. The diamond anvil cell (DAC) was constructed using a pair of nature single diamond by A.V. Valkenburg at the National Bureau of Standards of the USA [7]. What's more, the subsequent development of beveled DAC by H.K. Mao and P.M. Bell made the pressure reaching to 172 GPa [8]. Up to now in the experiment the highest static pressure

reported was 750 GPa by a German group, which was achieved by hemispherical second-stage anvil method [9].

As one of the fundamental thermodynamic variable, the effect of pressure on matter at atomic scale can influence atoms distance and bonding patterns, electron delocalization, electron transfer among different atomic orbitals, exotic charge redistribution and modifying the chemical identity of atoms [10-11].

The most straightforward effect of pressure on materials is the decrease of the interatomic and intermolecular distances, which would result in the reduction of volume and the increase of density. The changing of the atomic distances can lead to the phase transition of the materials. In many cases, the high-pressure phase can be recovered when the pressure is released, thus it opens a new way to the metastable phase at ambient pressure [12].

The electron density will increase by applying the pressure, which will lead to the change of delocalized electron. As a result, the pressure induced energy band broadens, gap closure and metallization will happen. In principle, under sufficient high pressure all insulators could become conductors. Furthermore, many of these conductors can show superconducting behavior after metallization. The halogen elements of iodine and bromine, the chalcogen elements of sulfur and oxygen are undergone metallization and the following superconductivity with the applying of pressure [13].

The energetic ordering of the outer atomic orbitals such as  $s$  and  $p$  orbitals may be changed by the applying of pressure. As a consequence, the occupied electrons can be transferred to unoccupied orbitals by orbital hybridization. The appearance of metal to semiconductor transition of lithium by the pressurization is a good example [14]. Furthermore, the insulating phase of Na is also originating from the hybridization [15].

Owing to the great effect of pressure on the determining the state of matter, pressure is also recognized as another dimension [11]. The ambient pressure is just deemed to be a special condition in this dimension. The exploration of new materials and new phenomenon in this dimension exhibit great interests. Since hydrogen is the first element of the periodic table, it should be the simplest one over all elements. However, the theoretical calculation on hydrogen under pressure is not as expected owing to its anharmonicity and notable quantum effects. The early prediction on the metallization of hydrogen under high pressure

of 25 GPa was reported by E. Wigner and H.B. Huntington in 1935 [16]. It was later turn out to be unrealized even the pressure is higher than 25 GPa in experiment. With the development of structure prediction science, the possible metallization pressure was predicted to exceeding 500 GPa, which cannot realized in the present experiment conditions. Furthermore, according to the BCS theory the calculated transition temperature ( $T_c$ ) can reach more than 300 K under 500 GPa [17, 18]. Thus, the high pressure science may play a significant role in the realization of room temperature superconductor.

## 1.2 Superconductivity

### 1.2.1 The history of superconductivity

Superconductivity shows a phenomenon of matter with exactly zero electronic resistance and the expulsion of the magnetic flux field. This behavior was first observed when cooling mercury to low temperature of 4.2 K by H.K. Onnes in 1911 [19, 20]. Stimulated by the discovery of superconducting behavior, many scientists contributed their work on the understanding of the mechanisms and tried to develop a microscopic theory. In 1933, the behavior that superconductors expel the magnetic flux at the temperature lower than the critical temperature was observed by H. Meissner and R. Ochsenfeld, which later called the Meissner effect [21]. Later, the phenomenon of Meissner effect was explained by the developed phenomenological theory by F. London and H. London [22]. However, it was still a mystery for the microscopic mechanism of superconductivity. In 1950, the theory that through vibrational fields the interaction between electrons and the crystal lattice can mediate the superconductivity was built [23]. Things became clear until the year in 1957, J. Barden, L. Cooper and J.R. Schrieffer published a microscopic theory to explain the superconductivity, which later called the BCS theory and showed a deep insight into the phenomenon of superconductors in experiment [24]. Owing to the first successful quantum theory development to the superconductivity, they shared the 1972 Nobel Prize in physics.

Another breakthrough of the superconductivity was the discovery of layered ceramic materials La-Ba-Cu-O system with  $T_c$  of 35 K in 1986 by J.G. Bednorz and K.A. Muller, who awarded the Nobel Prize in physics of 1987 [25]. Subsequent experiments showed that the  $T_c$  of La-Ba-Cu-O system increased rapidly under the effect of pressure [26]. The exciting resulting was the later discovery of Y-Ba-Cu-O system superconductors, which showed the  $T_c$  of 93 K higher than liquid nitrogen [27]. These kinds of layered ceramic materials as cuprates later exhibited the  $T_c$  of 134 K at ambient and 164 K under high pressure, which kept the highest  $T_c$  of all materials until the recent discovery of hydrogen sulfide [28, 29]. The other kind of high  $T_c$  materials are Fe-based superconductors, which were first discovered in  $\text{LaO}_{1-x}\text{F}_x\text{FeAs}$  by H. Hosono group in 2008 [30]. Soon after that the  $T_c$  of iron-based superconductors have been raised to above 40 K by substitute of other elements at ambient pressure [31, 32]. The highest  $T_c$  of this group superconductor in bulk is 56 K in  $\text{Gd}_{1-x}\text{Th}_x\text{FeAsO}$  [33]. While the microscopic mechanism of the cuprate superconductors and iron-based superconductors cannot be explained by the BCS theory. So cuprates and iron superconductors belong to the unconventional superconductors.

In 2015, a high  $T_c$  of 203 K under the pressure of 150 GPa was observed on compressing  $\text{H}_2\text{S}$  by M.I. Eremets group [34]. The high  $T_c$  of this new discovery promotes scientists with great interests in the exploration of other hydrides under high pressure. Fig. 1-1 shows the highest  $T_c$  of the superconductors since the discovery of superconductivity.

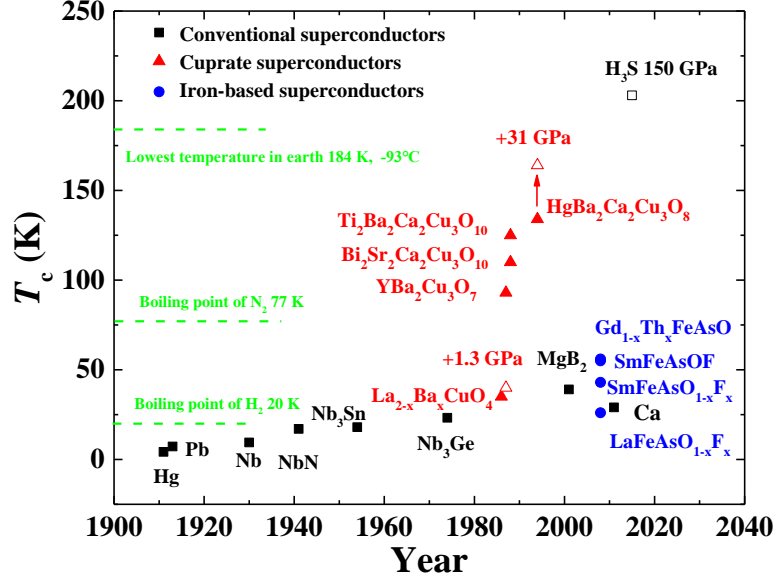


Fig. 1-1 the highest critical temperature of superconductors since the discovery of superconductivity as a function of time. The square, triangle and circle marks represent conventional superconductors, cuprate superconductors and iron-based superconductors, respectively. The open square and triangle marks exhibit the  $T_c$  observed with the effect of pressure. The green dash lines show the temperature of boiling point of  $H_2$ ,  $N_2$  and the lowest temperature in the earth as a reference.

### 1.2.2 BCS theory

The BCS theory demonstrates that it is more preferable that two electrons with opposite momenta and spin will form one pair below the critical temperature. The pair of electrons can be considered as a new particle, which is called Cooper pair. The pairing of electrons becomes the key idea of the theory. BCS theory quantitatively predicted a variety of properties of superconductivity, which include critical temperature, critical field, energy gap, isotope effect and special heat. In the limit of weak electron-phonon coupling, the BCS theory can describe the superconducting phenomenon and the critical temperature  $T_c$  as shown

$$T_c = 1.14 \left( \frac{\hbar\omega_D}{k_B} \right) \exp \left[ - \frac{1}{N(E_F)V_{eff}} \right] \quad (1)$$

Where  $h$  is the reduced Planck constant,  $\omega_D$  is the Debye frequency,  $k_B$  is the Boltzmann constant,  $N(E_F)$  is the density of states at the Fermi level and  $V_{\text{eff}}$  is the net attractive potential between the electron and electron pairs with positive [24].

The Cooper pair formed by the electrons near the Fermi level can be broken by the finite energy. Hence, there is an energy gap of  $2\Delta$  in the electronic excitation spectrum. The size of the energy gap decreases with the increasing of temperature and finally vanishes near  $T_c$ . The energy gap is given by BCS theory as

$$2\Delta(0) = 4h\omega_D \exp\left[-\frac{1}{N(E_F)V_{\text{eff}}}\right] \quad (2)$$

From the equation (1) and (2), the BCS theory regarding a fundamental constant at absolute zero Kelvin, the size of the energy gap can be described as

$$\frac{2\Delta(0)}{k_B T_c} = 3.52 \quad (3)$$

This prediction is well coincident with the experimental results for a large number of superconductors, such as Al and In which shown 3.4 and 3.6 respectively in experimentally [35].

The BCS theory also represents the temperature dependence of critical magnetic field,  $H_c$ . The relationship of critical magnetic field and temperature can be drawn as

$$H_c(T) \approx H_0 \left[1 - \left(\frac{T}{T_c}\right)^2\right] \quad (4)$$

Where  $H_0$  is the critical field at zero Kelvin.

In the BCS theory, the density of states  $N(E_F)$  and the attractive potential  $V_{\text{eff}}$  do not depend on the mass of the cation  $M$ . Thus  $T_c$  in the equation is given as

$$T_c \propto \langle \omega \rangle \propto M^{-\alpha} \quad (5)$$

Where  $M$  is the mass of the cation. Here  $\alpha$  can be described as

$$\alpha = -\frac{\delta \ln T_c}{\delta \ln M} \quad (6)$$

Since the Debye frequency  $\omega_D$  is proportional to  $M^{-\frac{1}{2}}$ ,

$$\omega_D \propto M^{-\frac{1}{2}} \quad (7)$$

Thus the isotope effect can be derived from the BCS theory.

$$T_c \propto \langle \omega \rangle \propto M^{-\frac{1}{2}} \quad (8)$$

Here  $\alpha \approx 0.5$ , which agrees well with the experimental value of  $\alpha$  in mercury.

### 1.3 Superconductivity under pressure

The pressure dependence of  $T_c$  can be originated from the superconductivity theories of weak-coupling BCS theory [24] or strong-coupling Eliashberg theory [36]. When a particular superconductor is considered, the pressure dependence of the microscopic parameters is needed to estimate  $T_c$  as a function of pressure.

According to the BCS theory,  $T_c$  can be written as

$$T_c = 1.14 \left(\frac{h}{k}\right) \langle \omega \rangle \exp\left[-\frac{1}{\lambda - \mu^*}\right] \quad (9)$$

Where  $h$  is Planck's constant,  $k$  is the lattice spring constant,  $\langle \omega \rangle$  is the average phonon frequency,  $\lambda$  is the electron-phonon coupling constant and  $\mu^*$  is the Coulomb pseudopotential. Since  $\mu^* \approx 0.1 \ll \lambda$ , thus,  $\lambda - \mu^* \approx \lambda$ . When the relation  $\omega_D \approx \langle \omega \rangle \approx \sqrt{k/M}$  is used,  $M \langle \omega^2 \rangle \approx M \langle \omega \rangle^2 \approx k$ . Furthermore,  $\lambda = \eta / M \langle \omega^2 \rangle = \eta / k$ . Thus,  $T_c$  can be expressed as

$$T_c = 1.14 \left(\frac{h}{k}\right) \sqrt{\frac{k}{M}} \exp\left[-\frac{k}{\eta}\right] \quad (10)$$

Where  $M$  is the mass of cation,  $\eta$  is the Hopfield parameter and  $\eta \equiv N(E_F) \langle I^2 \rangle$ , where  $\langle I^2 \rangle$  is the average square electronic matrix element. Due to the lattice stiffening and proportional behavior to  $(V_0/V)^\phi$ , the values of  $k$  and  $\eta$  would increase with the applying of pressure, respectively, where  $V_0$  and  $V$  are the volume of the matter at ambient and high pressure respectively and  $\phi$  is the empirical parameter with positive. Since the  $k$  in the exponent position, the effect of  $k$  dominates the pre-factor of  $\sqrt{k}$ . Hence, the effects of pressure is determined by the relative values of  $k$  and  $\eta$  [37-39].

In the case of simple *s*-electron and *p*-electron metals such as Al, In, Zn, Sn and Pb,  $k$  increase more rapidly than  $\eta$ , which results in a remarkable decrease of  $T_c$ . On the other hand, for the pressure dependence of transition metals, it is not clearly understood. The changes of  $T_c$  depend on the relative change of  $\eta$ . Pressure can induce structure, electronic or magnetic transition in some elements. With the effect of pressure, it is explained some elements show superconducting behavior at high pressure while do not be a superconductor at ambient pressure. Elements such as O, S, Br and I are insulator at ambient pressure and become superconductors under the pressure following the insulator-metal phase transition [40-44]. The superconductivity of Fe emerges after the magnetic behavior has been suppressed by pressure [45].

Fig. 1-2 shows the overview of superconductor at ambient pressure and achieved at high pressure throughout the periodic table. At ambient pressure, 29 elements show superconducting behavior when cooling to sufficiently low temperature. There are also 24 elements which are not superconducting at ambient, showing superconducting behavior under high pressure [46].

H																	He						
Li 30 GPa 14 K $T_c=0.4$ mK	Be																	B 250 GPa 11 K	C	N	O 100 GPa 0.6 K	F	Ne
Na	Mg																	Al $T_c=1.14$ K	Si 15.2 GPa 8.2 K	P 30 GPa 13 K	S 190 GPa 17.3 K	Cl	Ar
K	Ca 216 GPa 29 K	Sc 106 GPa 19.6 K	Ti 56 GPa 3.35 K $T_c=0.39$ K	V 120 GPa 16.5 K $T_c=5.30$ K	Cr	Mn	Fe 21 GPa 2.1 K	Co	Ni	Cu	Zn $T_c=0.075$ K	Ga 1.4 GPa 7 K $T_c=1.091$ K	Ge 11.5 GPa 5.35 K	As 32 GPa 2.4 K	Se 150 GPa 8 K	Br 100 GPa 1.4 K	Kr						
Rb	Sr 50 GPa 7 K	Y 115 GPa 19.5 K	Zr 30 GPa 11 K $T_c=0.546$ K	Nb 10 GPa 9.9 K $T_c=9.20$ K	Mo $T_c=0.92$ K	Tc $T_c=7.77$ K	Ru $T_c=0.51$ K	Rh $T_c=0.33$ mK	Pd	Ag	Cd $T_c=0.52$ K	In $T_c=3.4$ K	Sn 11.3 GPa 5.3 K $T_c=3.722$ K	Sb 25 GPa 3.9 K	Te 35 GPa 7.5 K	I 25 GPa 1.2 K	Xe						
Cs 12 GPa 1.3 K	Ba 18 GPa 5 K	La 15 GPa 13 K $T_c=6.00$ K	Hf 62 GPa 8.6 K $T_c=0.12$ K	Ta 43 GPa 4.5 K $T_c=4.483$ K	W $T_c=12$ mK	Re $T_c=1.4$ K	Os $T_c=0.66$ K	Ir $T_c=0.14$ K	Pt	Au	Hg $T_c=4.15$ K	Tl $T_c=2.39$ K	Pb $T_c=7.19$ K	Bi 9.1 GPa 8.5 K	Po	At	Rn						
Fr	Ra	Ac	Rf	Db	Sg																		
			Ce 5 GPa 1.7 K	Pr	Nd	Pm	Sm	Eu 142 GPa 2.75 K	Gd	Tb	Dy	Ho	Er	Tm	Yb	Lu 174 GPa 12.4 K							
			Th $T_c=1.37$ K	Pa $T_c=1.4$ K	U 1.2 GPa 2.4 K	Np	Pu	Am 6 GPa 2.2 K $T_c=0.79$ K	Cm	Bk	Cf	Es	Fm	Md	No	Lr							

Pressure required for maximum  $T_c$

Maximum  $T_c$

$T_c$  at ambient pressure

Superconducting at  $P = 0$

Superconducting only under pressure

Magnetic order at  $P = 0$

Fig. 1-2 the periodic table of superconductors in bulk at ambient and sufficiently high pressure for the highest  $T_c$  observed [46].

## 1.4 Superconductivity of hydrogen and hydrides

The exploration to the metallization of hydrogen under high pressure is derived from the theory work by E. Wigner and H.B. Huntington [16]. In their prediction, a body-centered lattice of hydrogen was predicted to show the possibility of metallization under high pressure that cannot obtain at that time. The development of hydrogen under high pressure was slow until the establishment of BCS theory. According to the BCS theory, hydrogen is the lightest elements in the periodic table and thus shows the high phonon frequency and possible the highest critical temperature. When the metallic modification of hydrogen is applied by the BCS theory, the energy of ionic hydrogen vibrations would be so high. Thus, the hydrogen could be a high temperature superconductor, which is predicted by N.W. Ashcroft in 1968 [47]. According to the quantum mechanics calculations, the molecular hydrogen would form a metallic state and become a

superconductor with the  $T_c$  of 242 K at 450 GPa [48]. While the molecular hydrogen becomes atomic hydrogen under 500 GPa with a  $T_c$  of 356 K [17, 18]. However, even the metallization of pure hydrogen is different to achieve in the experiment. Fig. 1-3 shows the pressure temperature phase diagram of hydrogen [49]. There are two ways to achieve the metallic hydrogen: pathway I and pathway II [50]. In pathway I, the high pressure was applied to hydrogen at relatively low temperature. As a consequence, four main phases were observed up to now, which were hexagonal close packed (HCP), the broken symmetry phase (BSP), the hydrogen-A phase and H<sub>2</sub>-PRE. In the pathway II, the metallization of hydrogen could be obtained at high temperature and pressure in the liquid phase, which is called plasma phase transition (PPT) predicted by M.A. Morales [51].

In the experiment, the conductive dense hydrogen was reported by M.I. Eremets [52]. While a serious criticism to their work has been presented [53]. Recently R.P. Dias and I.F. Silvera reported the observation of metallic hydrogen under the pressure of 495 GPa [49]. However, the debates existed related to the pressure region, the possible coating materials showing metallic luster and insufficient evidence [54, 55].

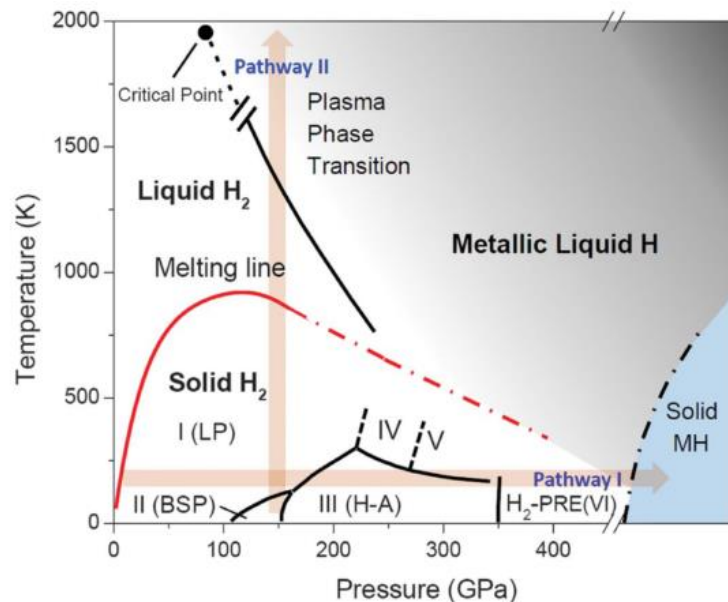


Fig. 1-3 Pressure versus temperature phase diagram of hydrogen [49].

Due to the inaccessible high pressure for the metallization of hydrogen at present experimental condition, the idea on the metallic and superconducting hydrogen was extended to mainly covalent hydrides, in which a chemical hydrogen has undergone by the so called “pre-compression” from the relative heavier elements proposed by N.W. Ashcroft [56]. After that a lot of theoretical work has been done to explore the superconductivity of hydrides. Covalent hydrides of group 14 such as SiH<sub>4</sub>, GeH<sub>4</sub>, SnH<sub>4</sub> have been extensively investigated. The high-pressure phases of silane were predicted to be metallic and showed superconducting behavior with the critical temperature ( $T_c$ ) from 12 K to 50 K under high pressure in several separate calculation results [57-60]. GeH<sub>4</sub> and SnH<sub>4</sub> were also predicted to be metallic under compression and even possible superconductor with  $T_c$  of 64 K at 220 GPa and 80 K at 120 GPa, respectively [61-63]. Later, the calculations of possible hydrides under high pressure were extended to other groups [64]. Many hydrogen-rich hydrides show high  $T_c$  above 200 K like, (H<sub>2</sub>S)<sub>2</sub>H<sub>2</sub> with  $T_c$  of 204 K at 200 GPa [65], CaH<sub>6</sub> with  $T_c$  of 235 K at 150 GPa [66], MgH<sub>6</sub> with  $T_c$  of 260 K at 300 GPa [67], YH<sub>6</sub> with  $T_c$  of 264 K at 120 GPa [68], YH<sub>10</sub> with  $T_c$  of 280 K at 210 GPa, and LaH<sub>10</sub> with  $T_c$  of 305 K at 250 GPa [69]. Some of the theoretical results are listed in the Table 1. From the table we can see, with the increase of hydrogen coordination number, the hydrides show the  $T_c$  increase tendency. Especially, the metal hydrides with the hydrogen number higher than 6. In CaH<sub>6</sub>, YH<sub>6</sub> and MgH<sub>6</sub>, 24 hydrogen atoms form sodalite-like cage sublattice centered Ca, Y or Mg atoms with bcc structure. While in the YH<sub>10</sub> and LaH<sub>10</sub> systems, the centered Y or La is surrounded by 32 hydrogen atoms to exhibit a sodalite-like cage fcc structure. Fig. 1-4 shows the possible crystal structure of LiH<sub>10</sub> (A, C) and CaH<sub>6</sub> (B, D).

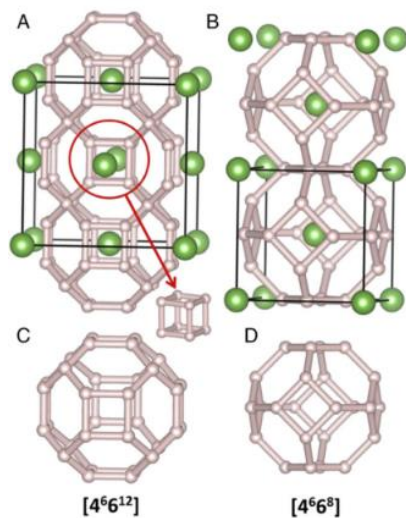


Fig. 1-4 the crystal structure of LaH<sub>10</sub> (A, C) and CaH<sub>6</sub> (B, D) [69].

Table 1 the theoretical prediction of hydrides with  $T_c$  and pressure region.

Hydrides	$T_c$ (K)	Pressure region	Reference
GaH <sub>3</sub>	76-86	160 GPa	70
PH <sub>3</sub>	83	200 GPa	71
Si <sub>2</sub> H <sub>6</sub>	139	275 GPa	72
SiH <sub>4</sub>	50	125 GPa	57
GeH <sub>4</sub>	64	220 GPa	61
GeH <sub>4</sub> (H <sub>2</sub> ) <sub>2</sub>	76-90	250 GPa	73
SiH <sub>4</sub> (H <sub>2</sub> ) <sub>2</sub>	98-107	250 GPa	74
(H <sub>2</sub> S) <sub>2</sub> H <sub>2</sub>	191-204	200 GPa	65
CaH <sub>6</sub>	220-235	150 GPa	66
MgH <sub>6</sub>	260	300 GPa	67
YH <sub>6</sub>	251-264	120 GPa	69
LaH <sub>10</sub>	274-286	210 GPa	69
YH <sub>10</sub>	305-326	250 GPa	69

In the experimental work on the searching for superconductivity of hydrides, silane was reported the transformation from insulating molecular to metal at 50 GPa and become

superconducting at the critical temperature of 17 K at 96 and 120 GPa firstly as shown in Fig. 1-5 (a) [75]. Though controversies existed on the decompression of silane to silicon and hydrogen above 50 GPa at room temperature and the metallization and superconductivity may come from the metal hydrides, which was formed by the decompression of hydrogen with the gasket material rhenium or the electrode material platinum [76-78]. Another hydride showing the superconducting behavior was sulfur hydride system with the  $T_c$  of surprising 203 K under the pressure of 150 GPa as shown in Fig 1-5 (b) [31]. Later, the crystal structure of the superconducting phase of hydrogen sulfide in its normal state and the superconducting state were observed by the synchrotron radiation X-ray diffraction (XRD) with a body center cubic (bcc) structure of  $H_3S$  [79]. The high  $T_c$  of hydrogen sulfide, which higher than the coolest observed temperature in the earth inspired scientists to explore more hydrogen-rich hydrides by means of measurements [80]. The stable high-pressure phase of the H-S system was obtained from the chemical reaction of sulfur and hydrogen under high pressure with laser heating, which enriches the research of high superconductivity [81].

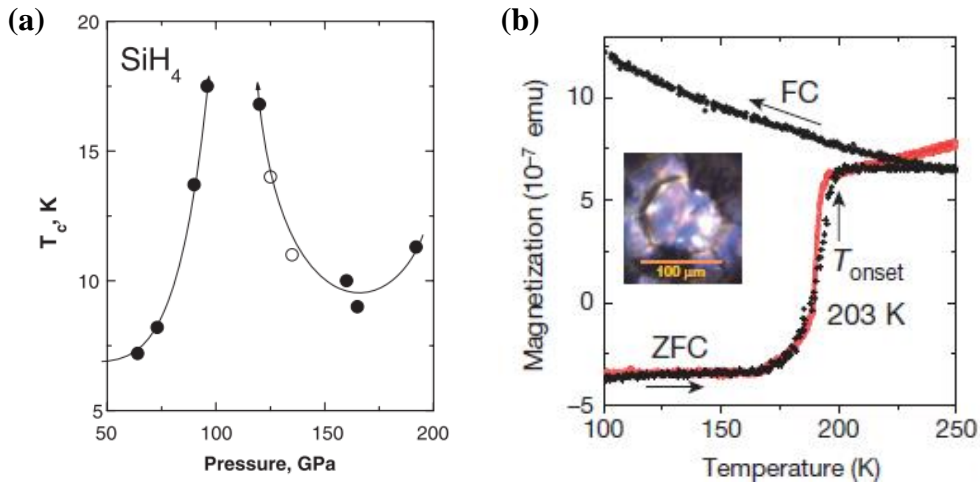


Fig. 1-5 the pressure dependence of  $T_c$  of  $SiH_4$  (a) and the onset  $T_c$  of sulfur hydride at high pressure (b) [75, 31].

Transition metal hydrides usually contain interstitial hydrogen atoms occupying octahedral or tetrahedral sites of the close packed structures with a signally rich variety of hydrogen coordination modes ranging from two-fold to nine-fold [82]. One of the hydride,

BaReH<sub>9</sub> demonstrates the high hydrogen density at ambient pressure, which is approximately twice than that of the liquid hydrogen [83, 84]. The hydrogen to metal ratio with 4.5 of this hydride is the highest so far. Recently this hydride BaReH<sub>9</sub> was reported to exhibit metallic behavior and furthermore superconducting behavior at around 100 GPa with the  $T_c$  of 7 K as shown in Fig. 1-6 [85]. The results provide new ideas for the exploration of the nature of pure hydrogen with metallic state and the superconductivity.

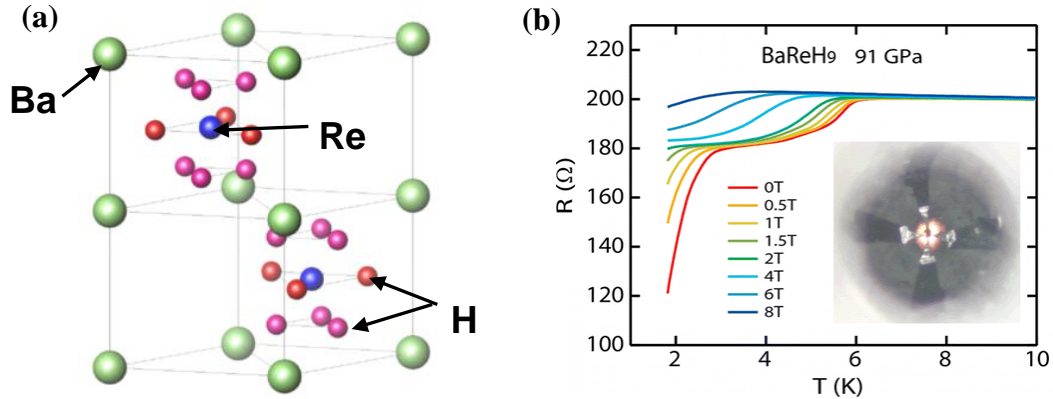


Fig. 1-6 the crystal structure of BaReH<sub>9</sub> with hexagonal structure (a) and the temperature dependence of resistance of BaReH<sub>9</sub> by applying the magnetic field to show the  $T_c$  at 91 GPa (b) [85].

Considering the alternative way to the metallic dense hydrogen and the possible high  $T_c$  in the hydrogen-rich hydrides, scientists also focused on the synthesis of polyhydrides under high pressure, which contain dense hydrogen. Furthermore, some unconventional stoichiometries novel polyhydrides shows stable under high pressure by using DAC. The polyhydrides of lithium hydrides were predicted and investigated by several groups [86-89]. The polyhydrides LiH<sub>x</sub>-II contains H<sub>2</sub> in the crystal lattice were detected below 62 GPa by laser heating lithium in hydrogen [87]. Several other new phases also confirmed by the high temperature and high-pressure method up to 180 GPa [88]. The lithium polyhydride LiH<sub>6</sub> containing H<sub>2</sub> units was synthesized in DAC above 130 GPa at 300 K from LiH and showed an insulating behavior up to 215 GPa [89]. The polyhydrides of sodium NaH<sub>3</sub> and NaH<sub>7</sub> were also synthesized in the laser heated DAC above 30 GPa and 2000 K [90]. The iridium hydride synthesized from iridium and hydrogen with very high

hydrogen content was reported up to 125 GPa. A phase transition in the metal lattice from the fcc to a distorted simple cubic phase is observed at 55 GPa [91]. The iron hydrides  $\text{FeH}_2$  and  $\text{FeH}_3$  were synthesized under high pressure by laser heating [92]. Furthermore, the iron pentahydride ( $\text{FeH}_5$ ) was synthesized by a direct reaction between iron and  $\text{H}_2$  above 130 GPa in a laser-heated diamond anvil cell. The results show that the structure of the superhydrides contain atomic hydrogen, whose structure resembles bulk atomic hydrogen [93]. The superhydrides of lanthanum  $\text{LaH}_{10+x}$  can be synthesized from La atoms in an fcc lattice and hydrogen at 170 GPa upon laser heating to about 1000 K. In the superhydrides, the La atom was surrounded by the cages of hydrogens occupied the fcc lattice position with a clathrate-like structure [94].

The progression in the discovery of these polyhydrides indicates a hydride with high H content, which possibly would be a real analog for atomic metal hydrogen. These syntheses of polyhydrides may provide new means for the pre-compress hydrogen molecules and facilitate the approaching to the metallic superconducting hydrogen at reduced pressures.

## References:

- [1] H.K. Mao, R.J. Hemley, The high-pressure dimension in earth and planetary science, *Proc. Natl. Acad. Sci.*, 104 (2007) 9114-9115.
- [2] J. Canton, Experiments to prove that water is not incompressible, *Phil. Trans. Roy. Soc.*, 52 (1762) 640-643.
- [3] P.W. Bridgman, *The physics of high pressure*, G. Bell and Sons, Ltd., London, 1949.
- [4] P.W. Bridgman, The measurement of high hydrostatic pressure I. A simple primary gauge, *Proceedings of the American Academy of Arts and Sciences*, 44 (1909) 201-217.
- [5] P.W. Bridgman, The measurement of high hydrostatic pressure II. A secondary mercury resistance gauge, *Proceedings of the American Academy of Arts and Sciences*, 44 (1909) 221-251.
- [6] P.W. Bridgman, An experimental determination of certain compressibilities, *Proceedings of the American Academy of Arts and Sciences*, 44(1909) 255-279.
- [7] C.E. Weir, A.V. Valkenburg, E.R. Lippincott, E.N. Bunting, Infrared studies in the 1 to 15 micro region to 30000 atmosphere, *Journal of research of the National Bureau of Standards A*, 63 (1959) 55-62.
- [8] H.K. Mao, P.M. Bell, High-pressure physics: sustained static generation of 1.36 to 1.72 Megabars, *Science*, 200 (1978) 1145-1147.
- [9] L. Dubrovinsky, N. Dubrovinskaia, E. Bykova, M. Bykov, V. Prakapenka, C. Prescher, K. Glazyrin, H.-P. Liermann, M. Hanfland, M. Ekholm, Q. Feng, L. V Pourovskii, M.I. Katsnelson, J.M. Wills, I.A. Abrikosov, The most incompressible metal osmium at static pressures above 750 gigapascals, *Nature*, 525 (2015) 226-229.
- [10] L. Zhang, Y. Wang, J. Lv, Y. Ma, Materials discovery at high pressures, *Nat. Rev. Mater.*, 2 (2017) 17005.
- [11] H. Mao, X. Chen, Y. Ding, Solids, liquids, and gases under high pressure, *Rev. Mod. Phys.*, 90 (2018) 15007.
- [12] F.J. Manjón, D. Errandonea, Pressure-induced structural phase transitions in materials and earth sciences, *Phys. Status. Solidi. Basic. Res.*, 246 (2009) 9-31.
- [13] K. Shimizu, Superconductivity from insulating elements under high pressure, *Physica C*, 514 (2015) 46-49

- [14] T. Matsuoka, K. Shimizu, Direct observation of a pressure-induced metal-to-semiconductor transition in lithium, *Nature*, 458 (2009) 186-189.
- [15] Y. Ma, M. Eremets, A.R. Oganov, Y. Xie, I. Trojan, S. Medvedev, A.O. Lyakhov, M. Valle, V. Prakapenka, Transparent dense sodium, *Nature*, 458 (2009) 182-185.
- [16] E. Wigner, H.B. Huntington, On the possibility of a metallic modification of hydrogen, *J. Chem. Phys.*, 3 (1935) 764-770.
- [17] J.M. McMahon, D.M. Ceperley, High-temperature superconductivity in atomic metallic hydrogen, *Phys. Rev. B*, 84 (2011) 1-8.
- [18] J.M. McMahon, M.A. Morales, C. Pierleoni, D.M. Ceperley, The properties of hydrogen and helium under extreme conditions, *Rev. Mod. Phys.*, 84 (2012) 1607-1653.
- [19] H.K. Onnes, *Leiden Comm.*, (1911) 122b-122c.
- [20] D. van Delft, P. Kes. The discovery of superconductivity. *Phys. Today*, 63 (2010) 38-42.
- [21] W. Meissner, R. Ochsenfeld, Ein neuer Effekt bei Eintritt der Supraleitfähigkeit, *Naturwissenschaften*, 21 (1933) 787-788.
- [22] F. London, H. London, The electromagnetic equations of the supraconductor, *Proceedings of the Royal Society of London, Series A, Mathematical and Physical Sciences*, 149 (1935) 71-88.
- [23] H. Frohlich, Theory of the superconducting state. I. the ground state at the absolute zero of temperature, *Phys. Rev.*, 79 (1950) 845-856.
- [24] J. Bardeen, L.N. Cooper, J.R. Schrieffer, Theory of superconductivity, *Phys. Rev.*, 108 (1957) 1175-1204.
- [25] J.G. Bednorz, K.A. Muller, Possible High  $T_c$  Superconductivity in the Ba-La-Cu-O System, *Z. Phys. B-Condensed Matter*, 64 (1986) 189-193.
- [26] C.W. Chu, P.H. Hor, R.L. Meng, L. Gao, Z.J. Huang, Y.Q. Wang, Evidence for superconductivity above 40 K in the La-Ba-Cu-O compound system, *Phys. Rev. Lett.*, 58 (1987) 405-407.
- [27] M.K. Wu, J.R. Ashburn, C.J. Torng, P.H. Hor, R.L. Meng, L. Gao, Z.J. Huang, Y.Q. Wang, C.W. Chu, Superconductivity at 93 K in a new mixed-phase Y-Ba-Cu-O compound system at ambient pressure, *Phys. Rev. Lett.*, 58 (1987) 908-910.

- [28] P. Dai, B. Chakoumakos, G. Sun, K. Wong, Y. Xin, D. Lu, Synthesis and neutron powder diffraction study of the superconductor  $\text{HgBa}_2\text{Ca}_2\text{Cu}_3\text{O}_{8+\delta}$  by Tl substitution, *Physica C*, 243 (1995) 201-206.
- [29] L. Gao, Y.Y. Xue, F. Chen, Q. Xiong, R.L. Meng, D. Ramirez, C.W. Chu, J.H. Eggert, H.K. Mao, Superconductivity up to 164 K in  $\text{HgBa}_2\text{Ca}_{m-1}\text{Cu}_m\text{O}_{2m+2+\delta}$  ( $m=1, 2,$  and  $3$ ) under quasihydrostatic pressures, *Phys. Rev. B*, 50 (1994) 4260-4263.
- [30] Y. Kamihara, T. Watanabe, M. Hirano, H. Hosono. Iron-based layered superconductor  $\text{LaO}_{1-x}\text{F}_x\text{FeAs}$  ( $x=0.05-0.12$ ) with  $T_c = 26$  K. *J Am. Chem. Soc.*, 130 (2008) 3296-3297.
- [31] X.H. Chen, T. Wu, G. Wu, R.H. Liu, H. Chen, D.F. Fang, Superconductivity at 43 K in  $\text{SmFeAsO}_{1-x}\text{F}_x$ . *Nature*, 453 (2008) 761-762.
- [32] H. Takahashi, K. Igawa, K. Arii, Y. Kamihara, M. Hirano, H. Hosono, Superconductivity at 43 K in an iron-based layered compound  $\text{LaO}_{1-x}\text{F}_x\text{FeAs}$ , *Nature*, 453 (2008) 376-378.
- [33] C. Wang, L. Li, S. Chi, Z. Zhu, Z. Ren, Y. Li, Y. Wang, X. Lin, Y. Luo, S. Jiang, X. Xu, G. Cao, Z. Xu, Thorium-doping-induced superconductivity up to 56 K in  $\text{Gd}_{1-x}\text{Th}_x\text{FeAsO}$ . *Europhys. Lett.*, 83 (2008) 67006.
- [34] A.P. Drozdov, M.I. Erements, I.A. Troyan, V. Ksenofontov, S.I. Shylin, Conventional superconductivity at 203 kelvin at high pressures in the sulfur hydride system, *Nature*, 525 (2015) 73-76.
- [35] N. W. Ashcroft and N. D. Mermin, *Solid State Physics*, Thomas Learning, Inc., United States, 1976.
- [36] G. M. Eliashberg, *Soviet Phys.-JEPT* 11, 696 (1960); 12, 1000 (1961).
- [37] B. Lorenz, C.W. Chu, High pressure effects on superconductivity, *Front. Supercond. Mater.*, (2005) 459-497.
- [38] J.S. Schilling, High pressure effects, *Hand book of high-temperature superconductivity*, (2007) 427-462.
- [39] J.S. Schilling, J.J. Hamlin, Recent studies in superconductivity at extreme pressures, *Journal of Physics: Conference Series*, 121 (2008) 052006.
- [40] K. Shimizu, K. Suhara, M.I. Erements, K. Amaya, Superconductivity in oxygen, *Nature*, 393 (1998) 767-769.

- [41] S. Kometani, M.I. Eremets, K. Shimizu, M. Kobayashi, K. Amaya, Observation of pressure-induced superconductivity of sulfur, *J. Phys. Soc. Jpn.*, 66 (1997) 2564-2565.
- [42] V.V. Struzhkin, R.J. Hemley, H.K. Mao, Y.A. Timofeef, Superconductivity at 10-17 K in compressed Sulphur, *Nature*, 390 (1997) 382-384.
- [43] K. Shimizu, K. Amaya, S. Endo, *Rev. High Press. Sci. Technol.*, 4 (1995) 498.
- [44] K. Shimizu, T. Yamauchi, N. Tamitani, N. Takeshita, M. Ishizuka, K. Amaya, S. Endo, The pressure-induced superconductivity of iodine, *J. Supercond.*, 7 (1994) 921-924.
- [45] K. Shimizu, T. Kimura, S. Furomoto, K. Takeda, K. Kontani, Y. Onuki, K. Amaya, Superconductivity in the non-magnetic state of iron under pressure., *Nature*, 412 (2001) 316-318.
- [46] J.J. Hamlin, Superconductivity in the metallic elements at high pressures, *Physica C*, 514 (2015) 59-76.
- [47] N.W. Ashcroft, Metallic Hydrogen: A High-Temperature Superconductor?, *Phys. Rev. Lett.*, 21 (1968) 1748-1749.
- [48] P. Cudazzo, G. Profeta, A. Sanna, A. Floris, A. Continenza, S. Massidda, E.K.U. Gross, Ab initio description of high-temperature superconductivity in dense molecular hydrogen, *Phys. Rev. Lett.*, 100 (2008) 1-4.
- [49] R.P. Dias, I.F. Silvera, Observation of the Wigner-Huntington transition to metallic hydrogen, *Science*, 355 (2017) 715-718.
- [50] I. Silvera, The insulator-metal transition in hydrogen, *Proc. Natl. Acad. Sci.*, 107 (2010) 12743-12744.
- [51] M.A. Morales, C. Pierleoni, E. Schwegler, D.M. Ceperley, Evidence for a first order liquid-liquid transition in high pressure hydrogen from ab-initio simulations. *Proc. Natl. Acad. Sci.*, 107 (2010):12799-12803.
- [52] M.I. Eremets, I. A. Troyan, Conductive dense hydrogen, *Nat. Mater.*, 10 (2011) 927-931.
- [53] W. Nellis, I. Silvera, Has Metallic Hydrogen Been Made in a Diamond Anvil Cell? [arXiv:1201.0407](https://arxiv.org/abs/1201.0407), 2013.
- [54] X.-D. Liu, P. Dalladay-Simpson, R.T. Howie, B. Li, E. Gregoryanz, Comment on “Observation of the Wigner-Huntington transition to metallic hydrogen”, *Science*, 357, 2286 (2017).

- [55] A.F. Goncharov, V.V. Struzhkin, Comment on “Observation of the Wigner-Huntington transition to metallic hydrogen”, *Science*, 357, 9736 (2017).
- [56] N.W. Ashcroft, Hydrogen dominant metallic alloys: High temperature superconductors?, *Phys. Rev. Lett.*, 92 (2004) 187001-187002.
- [57] Y. Yao, J.S. Tse, Y. Ma, K. Tanaka, Superconductivity in high-pressure SiH<sub>4</sub>, *Europhys. Lett.*, 78 (2007) 37003.
- [58] M. Martinez-Canales, A.R. Oganov, Y. Ma, Y. Yan, A.O. Lyakhov, A. Bergara. Novel structures and superconductivity of silane under pressure. *Phys. Rev. Lett.*, 102 (2009) 087005.
- [59] J. Feng, W. Grochala, T. Jaron, R. Hoffmann, A. Bergara, N.W. Ashcroft. Structures and potential superconductivity in SiH<sub>4</sub> at high pressure: En route to “metallic hydrogen”. *Phys. Rev. Lett.*, 96 (2006) 0170006.
- [60] C.J. Pickard, R.J. Needs. High-pressure phases of silane. *Phys. Rev. Lett.*, 97 (2006) 045504.
- [61] G. Gao, A.R. Oganov, A. Bergara, M. Martinez-Canales, T. Cui, T. Iitaka, Y. Ma, G. Zou, Superconducting high pressure phase of germane, *Phys. Rev. Lett.*, 101 (2008) 2-5.
- [62] J.S. Tse, Y. Yao, K. Tanaka. Novel superconductivity in metallic SnH<sub>4</sub> under high pressure. *Phys. Rev. Lett.*, 98 (2007) 067002-067004.
- [63] G. Gao, A.R. Oganov, P. Li, Z. Li, H. Wang, T. Cui, Y. Ma, A. Bergara, A.O. Lyakhov, T. Iitaka, G. Zou, High-pressure crystal structures and superconductivity of Stannane (SnH<sub>4</sub>), *Proc. Natl. Acad. Sci.*, 107 (2010) 1317-1320.
- [64] H. Wang, X. Li, G. Gao, Y. Li, Y. Ma, Hydrogen-rich superconductors at high pressures, *Advanced Rev.*, 8 (2018) 1-13.
- [65] D. Duan, Y. Liu, F. Tian, D. Li, X. Huang, Z. Zhao, H. Yu, B. Liu, W. Tian, T. Cui, Pressure-induced metallization of dense (H<sub>2</sub>S)<sub>2</sub>H<sub>2</sub> with high-  $T_c$  superconductivity, *Sci. Rep.*, 4 (2014) 6968.
- [66] H. Wang, J.S. Tse, K. Tanaka, T. Iitaka, Y. Ma, Superconductive sodalite-like clathrate calcium hydride at high pressures, *Proc. Natl. Acad. Sci.*, 109 (2012) 6463-6466.
- [67] X. Feng, J. Zhang, G. Gao, H. Liu, H. Wang, Compressed sodalite-like MgH<sub>6</sub> as a potential high-temperature superconductor, *RSC Adv.*, 5 (2015) 59292-59296.

- [68] Y. Li, J. Hao, H. Liu, J.S. Tse, Y. Wang, Y. Ma, Pressure-stabilized superconductive yttrium hydrides, *Sci. Rep.*, 5 (2015) 9948.
- [69] H. Liu, I.I. Naumov, R. Hoffmann, N.W. Ashcroft, R.J. Hemley, Potential high-  $T_c$  superconducting lanthanum and yttrium hydrides at high pressure, *Proc. Natl. Acad. Sci.*, 114 (2017) 6990-6995.
- [70] G. Gao, H. Wang, A. Bergara, Y. Li, G. Liu, Y. Ma, Metallic and superconducting gallane under high pressure, *Phys. Rev. B*, 84 (2011) 1-5.
- [71] H. Liu, Y. Li, G. Gao, J.S. Tse, I.I. Naumov, Crystal Structure and Superconductivity of  $\text{PH}_3$  at High Pressures, *J. Phys. Chem. C*, 120 (2016) 3458-3461.
- [72] X. Jin, X. Meng, Z. He, Y. Ma, B. Liu, T. Cui, G. Zou, H. Mao, Superconducting high-pressure phases of disilane, *Proc. Natl. Acad. Sci.*, 107 (2010) 9969-9973.
- [73] G. Zhong, C. Zhang, X. Chen, Y. Li, R. Zhang, H. Lin, Structural, electronic, dynamical, and superconducting properties in dense  $\text{GeH}_4(\text{H}_2)_2$ , *J. Phys. Chem. C*, 116 (2012) 5225-5234.
- [74] Y. Li, G. Gao, Y. Xie, Y. Ma, T. Cui, G. Zou, Superconductivity at approximately 100 K in dense  $\text{SiH}_4(\text{H}_2)_2$  predicted by first principles., *Proc. Natl. Acad. Sci.*, 107 (2010) 15708-15711.
- [75] M.I. Eremets, I.A. Trojan, J.S. Tse, Y. Yao, Superconductivity in hydrogen dominant materials: silane, *Science*, 319 (2008) 1506-1510.
- [76] O. Degtyareva, J.E. Proctor, C.L. Guillaume, E. Gregoryanz, M. Hanfland, Formation of transition metal hydrides at high pressures, *Solid State Commun.*, 149 (2009) 1583-1586.
- [77] T.A. Strobel, A.F. Goncharov, C.T. Seagle, Z. Liu, M. Somayazulu, V. V. Struzhkin, R.J. Hemley, High-pressure study of silane to 150 GPa, *Phys. Rev. B*, 83 (2011) 1-14.
- [78] M. Hanfland, J.E. Proctor, C.L. Guillaume, O. Degtyareva, E. Gregoryanz, High-pressure synthesis, amorphization, and decomposition of silane, *Phys. Rev. Lett.*, 106 (2011) 2-5.
- [79] M. Einaga, M. Sakata, T. Ishikawa, K. Shimizu, M.I. Eremets, A. Drozdov, I. Troyan, N. Hirao, Y. Ohishi, Crystal structure of the superconducting phase of sulfur hydride, *Nature physics*, 12 (2016) 835-838.

- [80] M. Einaga, M. Sakata, A. Masuda, H. Nakao, K. Shimizu, Two-year progress in experimental investigation on high-temperature superconductivity of sulfur hydride crystals, *Jpn. J. of App. Phys.*, 56(2017) 05FA13.
- [81] A.F. Goncharov, S.S. Lobanov, V.B. Prakapenka, E. Greenberg, Stable high-pressure phases in the H-S system determined by chemically reacting hydrogen and sulfur, *Phys. Rev. B*, 95 (2017) 1-5.
- [82] S. Takagi, S.I. Orimo, Recent progress in hydrogen-rich materials from the perspective of bonding flexibility of hydrogen, *Scr. Mater.*, 109 (2015) 1-5.
- [83] E.A. Vinitsky, T. Muramatsu, M. Somayazulu, W.K. Wanene, Z. Liu, D. Chandra, R.J. Hemley, Structural, vibrational, and electronic properties of BaReH<sub>9</sub> under pressure, *J. Phys. Condens. Matter*, 28 (2016) 505701.
- [84] D.J. Singh, M. Gupta, R. Gupta, Cohesion of BaReH<sub>9</sub> and BaMnH<sub>9</sub>: Density functional calculation and prediction of (MnH<sub>9</sub>)<sup>2-</sup> salts, *Phys. Rev. B*, 75 (2007) 035103.
- [85] T. Muramatsu, W.K. Wanene, M. Somayazulu, E. Vinitsky, D. Chandra, T.A. Strobel, V. V Struzhkin, R.J. Hemley, Metallization and superconductivity in the hydrogen-rich ionic salt BaReH<sub>9</sub>, *J. Phys. Chem. C.*, 119 (2015) 18007-18013.
- [86] E. Zurek, R. Hoffmann, N.W. Ashcroft, A.R. Oganov, A.O. Lyakhov, A little bit of lithium does a lot for hydrogen, *Proc. Natl. Acad. Sci.*, 106 (2009) 17640-17643.
- [87] K. Kuno, T. Matsuoka, T. Nakagawa, N. Hirao, Y. Ohishi, K. Shimizu, K. Takahama, K. Ohta, M. Sakata, Y. Nakamoto, T. Kume, S. Sasaki, Heating of Li in hydrogen: possible synthesis of LiH<sub>x</sub>, *High Press. Res.*, 35 (2015) 16-21.
- [88] T. Matsuoka, K. Kuno, K. Ohta, M. Sakata, Y. Nakamoto, N. Hirao, Y. Ohishi, K. Shimizu, T. Kume, S. Sasaki, Lithium polyhydrides synthesized under high pressure and high temperature, *J. Raman Spectrosc.*, 48 (2017) 1222-1228.
- [89] C. Pépin, P. Loubeyre, F. Occelli, P. Dumas, Synthesis of lithium polyhydrides above 130 GPa at 300 K., *Proc. Natl. Acad. Sci.*, 112 (2015) 7673-7676.
- [90] V.V. Struzhkin, D. Kim, E. Stavrou, T. Muramatsu, H. Mao, C.J. Pickard, R.J. Needs, V.B. Prakapenka, A.F. Goncharov, Synthesis of Sodium Polyhydrides at High Pressures, *Nature Commun.*, 7 (2014) 1-16.

- [91] T. Scheler, M. Marques, Z. Konopkova, C.L. Guillaume, R.T. Howie, E. Gregoryanz, High-pressure synthesis and characterization of iridium trihydride, *Phys. Rev. Lett.*, 111 (2013) 1-5.
- [92] C.M. Pépin, A. Dewaele, G. Geneste, P. Loubeyre, M. Mezouar, New iron hydrides under high pressure, *Phys. Rev. Lett.*, 113 (2014) 1-5.
- [93] C.M. Pépin, G. Geneste, A. Dewaele, M. Mezouar, P. Loubeyre, Synthesis of FeH<sub>5</sub>: A layered structure with atomic hydrogen slabs, *Science*, 357 (2017) 382-385.
- [94] Z.M. Geballe, H. Liu, A.K. Mishra, M. Ahart, M. Somayazulu, Y. Meng, M. Baldini, R.J. Hemley, Synthesis and Stability of Lanthanum Superhydrides, *Angew. Chemie - Int. Ed.*, 57 (2018) 688-692.

## Chapter 2. Experimental methods

In this chapter, the high pressure generated apparatus diamond anvil cell (DAC) will be introduced. The details of the preparation of the DAC, the preparation of sample and the method of pressure determination are also shown. At last, the measurements of the DAC by electrical resistance, low temperature cooling and the synchrotron powder XRD will be presented.

### 2.1 Diamond anvil cell (DAC)

The diamond anvil cell (DAC) is an apparatus that consisted of two opposing diamonds to generate hundreds of gigapascal (GPa) of static high pressure as shown in Fig. 2-1. The three basic components of the DAC are a pair of opposing diamonds, a confining gasket between the diamonds and the sample hole. The pressure is generated by the squeezing of a pair of diamonds with screws through mechanical rotation. The thickness of the gasket and sample decreases with the pressurization process. Due to the transparent property of diamond, the DAC can provide transparent windows for optical observation and a broad range of techniques and measurement in situ as shown in Fig. 2-2. With these techniques and measurements, the research of phase structure, electronic characterization, vibrational and magnetic properties can be conducted with an extensive range of pressure conditions. Since the DAC was designed in 1950s, a lot of developments have been done for the optimization of pressure, temperature, sample chamber and characterization [1-3]. Thus, DAC becomes a powerful tool in the study of ultrahigh static pressure.

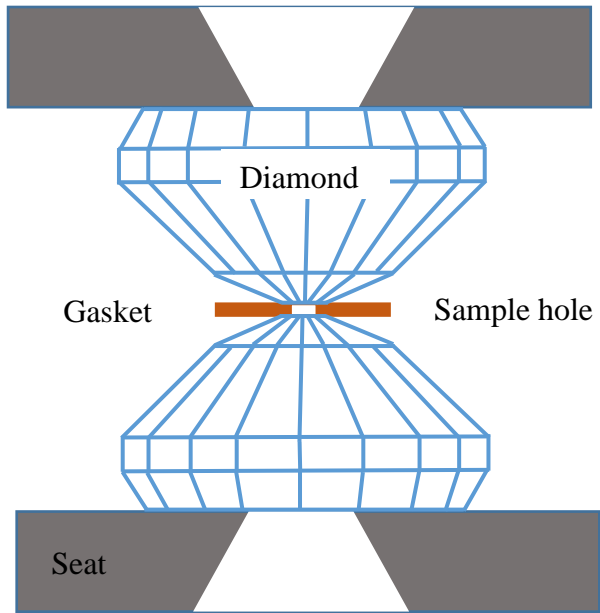


Fig. 2-1 the sketch of the main part of DAC.

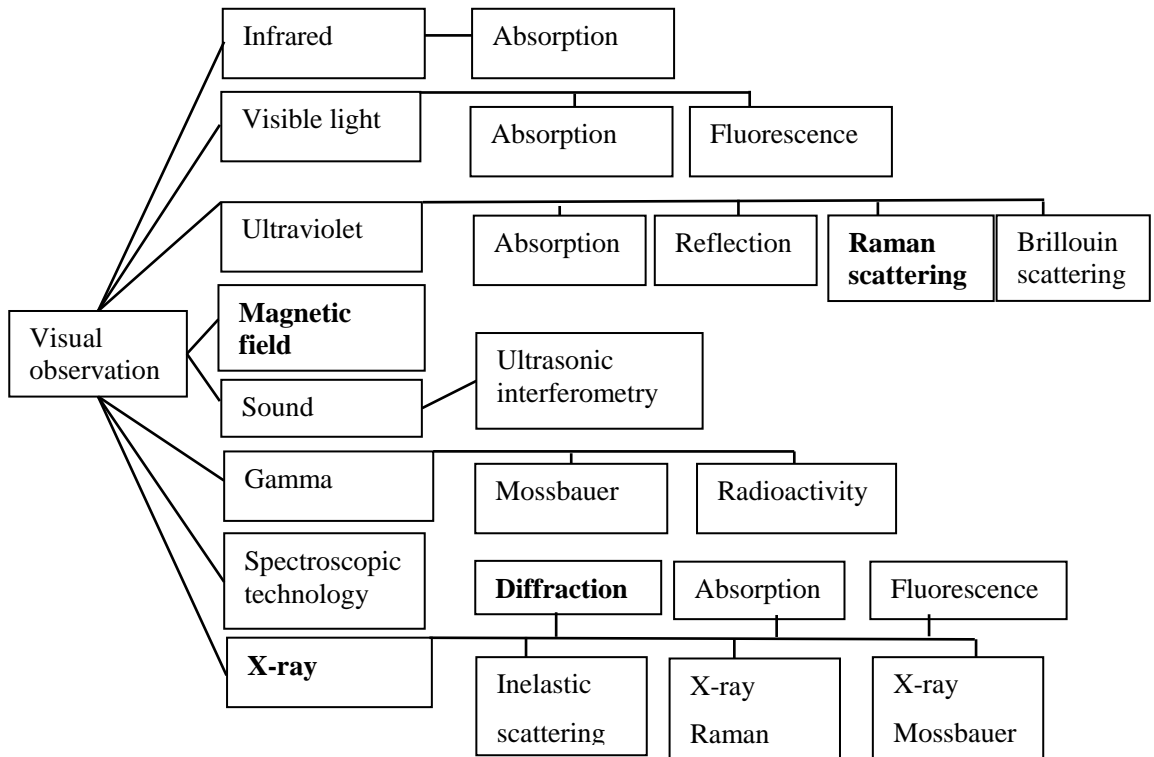


Fig. 2-2 the experiment techniques and measurements realized by DAC. Used techniques in this thesis in bold.

The diamond is the most important part of the DAC apparatus. Usually a pair of single crystal diamonds is used in the DAC with the mass less than 0.5 carats. The single crystal diamond shows outstanding properties of high hardness, fracture toughness, high melting temperature, high thermal conductivity, high magnetic field compatibility and low friction. Furthermore, owing to the superior chemical inertness the diamond makes the target samples away from contaminating even though it is part of the sample chamber that contacts a wide range of materials. In a typical diamond, one side is a small culet and the other side is a large table facet. The flat diamond anvil is proficiently cut parallel to the (110) plane. The culet size of the diamond ranges from 20  $\mu\text{m}$  to near several millimeters as presented in Fig. 2-3 (a), which is depended on the target pressure and the experimental conditions. In order to obtain a higher pressure, the beveled diamond anvil was designed by H.K. Mao [4]. The beveled angle usually keeps between 7 and 8.5 degrees as shown in Fig 2-3 (b). In this experiment, the culet size of the diamond is 100-300  $\mu\text{m}$  with the beveled angle of 8 degrees as shown in Fig. 2-4.

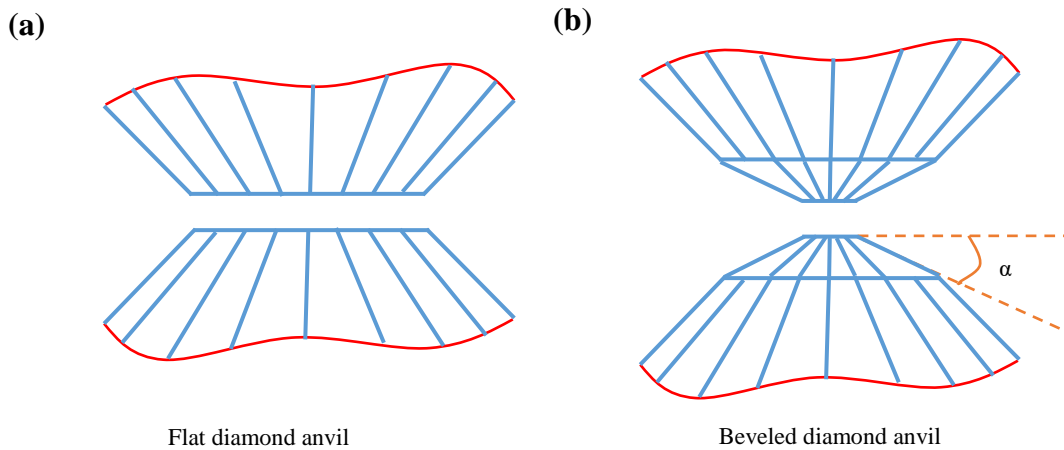


Fig. 2-3 the shape of the diamond: (a) flat diamond anvil and (b) beveled diamond anvil with the beveled angle of  $\alpha$ .

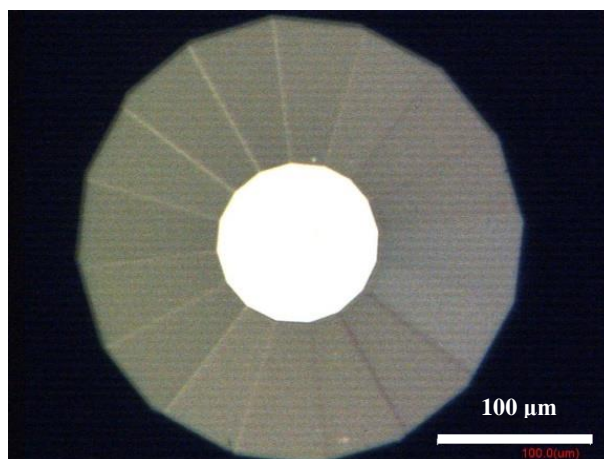


Fig. 2-4 the diamond used in this experiment: beveled 100-300  $\mu\text{m}$  culet size with angle of 8 degrees.

When the opposing beveled diamonds compressed to each other, the culet regions will bend outward to show a cup shape due to the deformation under the high pressure [3, 5, 6]. Fig. 2-5 presents the research on the thickness of the gasket between two diamonds and the deformation of the culet diamond area [3]. The gasket exhibits convex shape at the culet area when the pressure is above 170 GPa. The deformation of the 20  $\mu\text{m}$  culet is 1.5  $\mu\text{m}$  at the center position of the culet ( $h_2$  in Fig. 2-5c) when the pressure is 400 GPa. Furthermore, the pressure distribution depends on the distance to the center of the culet. Fig. 2-6 points out the 20-300  $\mu\text{m}$  beveled diamond culet pressure distribution. The pressure is more concentrated on the culet region at all the checked pressure section. The research on the changes of culet under high pressure and the pressure distribution is propitious to the understanding of the sample inside the DAC.

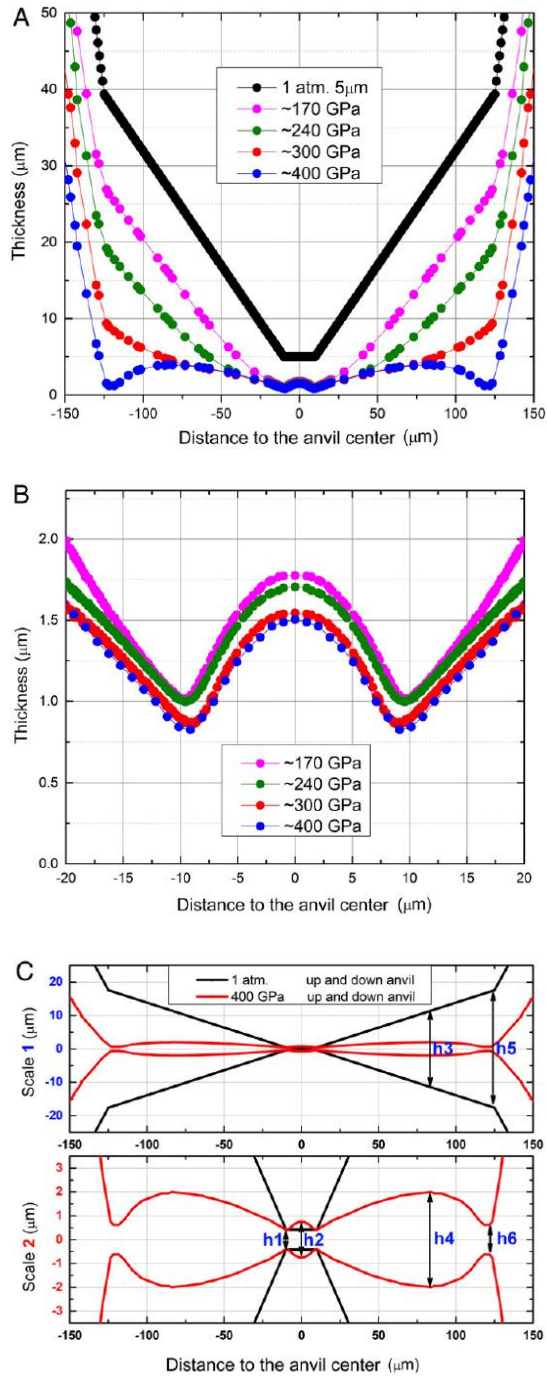


Fig. 2-5 the deformation of gasket between two diamonds: the thickness of the gasket with the distance to the center of culet at large region (a) and culet region (b). The deformation of the culet region at ambient and 400 GPa [3].

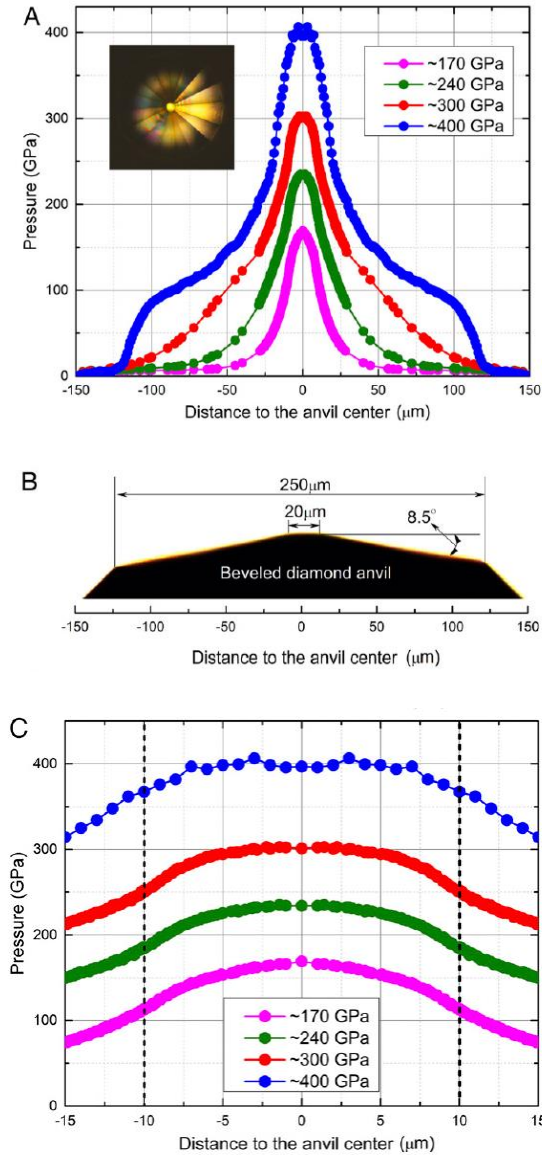


Fig. 2-6 the pressure distribution of the diamond under various pressures [3].

The diamonds are mounted on the supporting seat to transmit the force from the body of the DAC to the diamonds. Usually the seat needs to be hard enough in order to withstand the high pressure and well ductile to prevent the occurrence of cracks. Thus, the chosen materials of the seat are important for the experiment. For example, tungsten carbide due to its perfect strength, Cu-Be due to its nonmagnetic property to reduce the background [7]. The surface of the seat should be polished by the diamond grinding paper to remove the possible scratch. In the center position of the seat, a tapered opening is designed for the

optical observation and measurements. Usually, the bottom diamond mounted on a flat seat as shown in Fig. 2-7 (a), which is fixed on the DAC body. While the top diamond seat shows hemisphere shape in order to adjust the parallelism of the two diamond culets as shown in Fig. 2-7 (b).

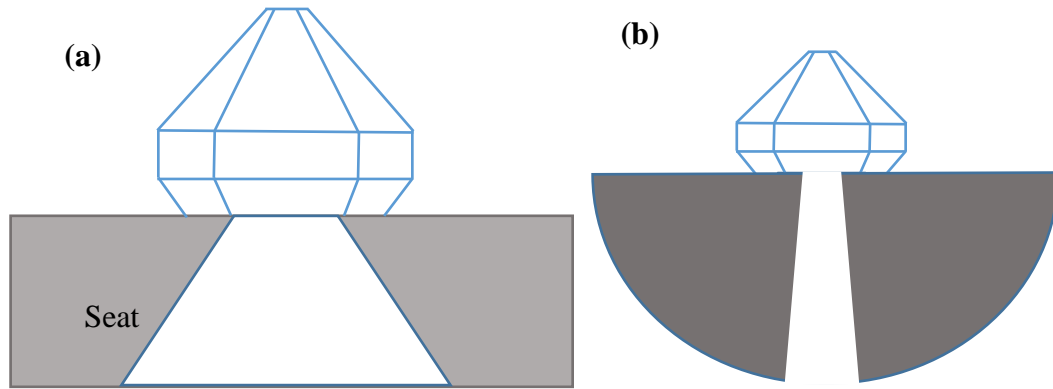


Fig. 2-7 the sketch of the diamond and the seat: (a) bottom diamond and the flat seat, (b) top diamond and the hemisphere seat.

There are various kinds of DACs designed by researchers for different purposes [8-13]. In this experiment, the DAC body was designed for electrical resistance in the Shimizu laboratory as described in Fig. 2-8 [5]. The main body of the DAC is made by Cu-Be alloy, which shows good thermal conductivity and low magnetization even at 1 K. The nonmagnetic DAC even in low temperature can avoid to the suppression of superconductivity. In this DAC, there is a plastic ring between the nut and the piston to retard the pressure change during the DAC cooling to low temperature. Thus, the DAC can keep the pressure at room temperature and low temperature with an error bar of several percentage even above 50 GPa.

In order to prevent the failure of the diamond and achieve high pressure, the alignment of the diamonds must be perfect with the culets parallel to each other. What's more, a stable and reproducible alignment must be obtained during the preparation of gasket, opening the DAC, loading the sample in the gasket and the compression to high pressure. The most useful method of applying the force to the diamond is mechanically tightening the screws.

The constant pressure can generate in the DAC body and the force can keep steadily for more than decades.

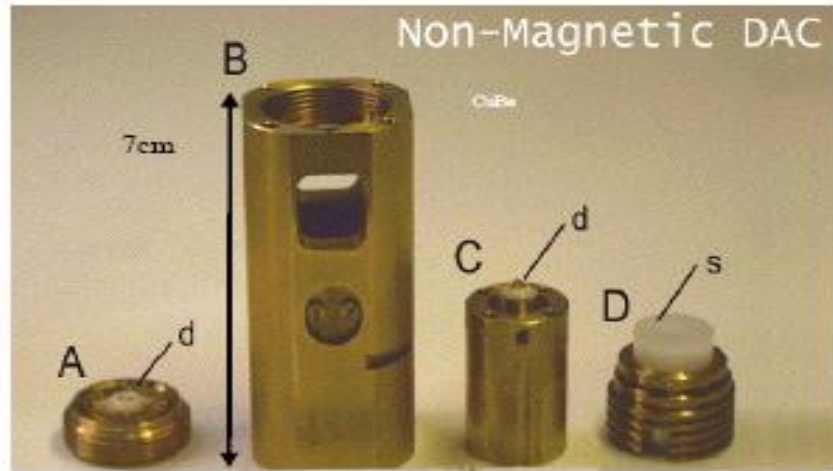


Fig. 2-8 the DAC used for electrical resistance measurement.

For the synchrotron powder XRD, a large angle tapered opening in the supporting seat is needed. Thus, the larger size DAC is used as shown in Fig. 2-9. Due to the large size of the DAC body, the low temperature measurement is avoided in this type. In both types of DACs, the pressure is generated by rotating the nut on the bottom with a gearbox as shown in Fig. 2-10.



Fig. 2-9 The DAC used for synchrotron powder XRD.



Fig. 2-10 the gearbox for rotating the nut of DAC.

## 2.2 Preparation for DAC

The diamonds must be cleaned completely under the microscope to remove the possible dust by cotton swabs absorbed methanol or ethanol before mounting on the supporting seat. After the table facet of diamonds and the seats were thoroughly cleaned, the diamond was put on the seat. The adjustment of the relative position of the diamond and the seat can be done in the holder as shown in Fig. 2-11. Since the tapered opening hole locates right in the center of the seat, the culet position of the diamond should be set in the center of the tapered opening. The diamonds were glued on the seats by epoxy (STYCAST 2850 black and catalyst 23LV) with a heating temperature of 65 °C for 2 h or room temperature for 12 h. After the diamonds were fixed on the DAC, they were aligned in the lateral direction by the fixing nuts from four directions. The parallelism of the diamond culets were aligned by adjusting the hemisphere nuts on the top part of the DAC. A perfect parallelism of culets can be achieved by showing the same color of the interference fringes when the two diamonds approach to each other. The proper alignment of the diamonds is an important factor to the success of the experiment, especially in high pressure experiment. Usually the displacement of the two diamonds should keep within 5  $\mu\text{m}$  in 100  $\mu\text{m}$  culet size. Fig. 2-12 shows the position of the two diamond culets.

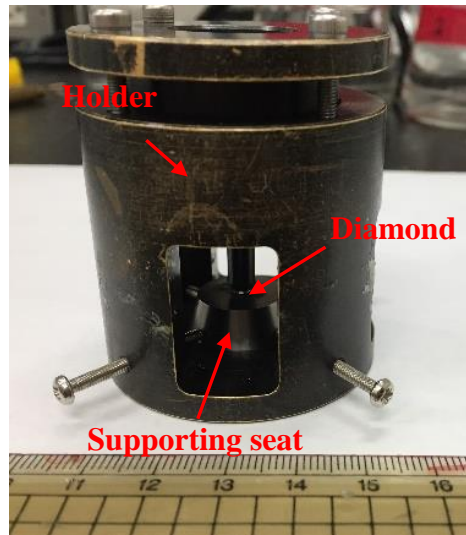


Fig. 2-11 the holder for fixing the diamond on the supporting seat.

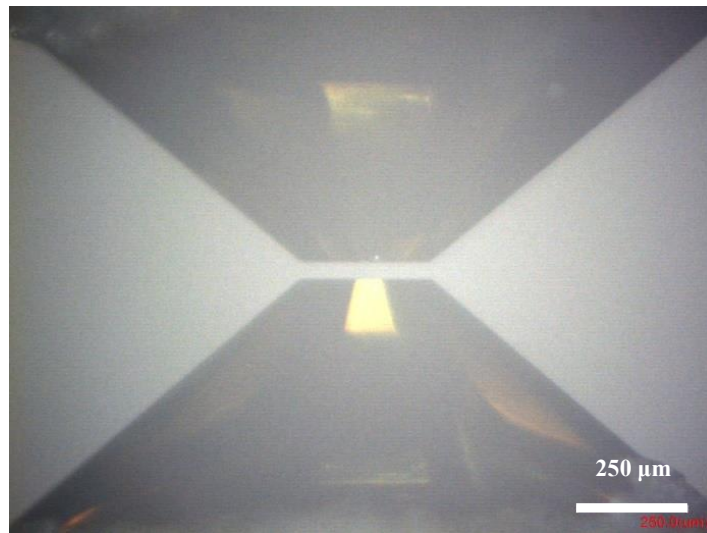


Fig. 2-12 the diamond culets with proper position.

In the high-pressure experiment, the proper choice of the gasket materials is extremely vital. The gasket is used to support the diamond and as the sample chamber for loading sample, ruby and pressure medium. The gasket material should be modest hardness and ductility. If the hardness of the gasket material is not enough, it cannot support the high pressure during the experiment. If the material is not ductile enough, the gasket may produce cracks or be brittle, which results in the failure of diamonds.

Stainless is the most common material for pressure lower than 50 GPa. Rhenium is available in high pressure experiment due to its low magnetism and high hardness. Beryllium is widely used in the synchrotron XRD experiment owing to its low XRD signal. The CuBe alloy gasket is chosen in the high pressure hydrogen experiment since the chemical inertness of CuBe to hydrogen. Tungsten gasket is also common in high pressure experiment.

In this experiment, Re was chosen owing to its low magnetism and high hardness. The rhenium gasket with a thickness of 250  $\mu\text{m}$  was cut to 0.5 $\times$ 0.5 mm size and then glued on the holder as shown in Fig. 2-13, which is used to support the gasket. During the pre-indentation of the gasket, the reduction of the thickness should be controlled step by step in order to prevent the cold-welding of the diamond to the gasket.

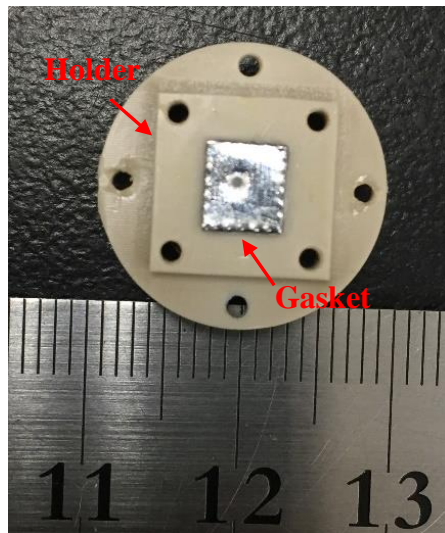


Fig. 2-13 the rhenium gasket fixed on the holder.

In this experiment, we not only need to obtain high pressure, but also measure the in situ electrical resistance under high pressure. Thus, the configuration of the probe electrodes is an important step. Two attempts are tried in this thesis. The sketches of the setting method 1 and 2 on the gasket are shown in Fig. 2-14 (a) and (b), respectively. The rhenium plate with thickness of 250  $\mu\text{m}$  pre-indented to 25  $\mu\text{m}$  was chosen as a gasket. A hole of 130  $\mu\text{m}$  diameter was drilled in the center of the pre-indented rhenium gasket. Making the insulation between the metal gasket and the electrodes would be the essential for performing the resistance measurement. Thus, a scotch tape was put on the gasket. In

method 1, the mixtures of *c*-BN and epoxy were put on the drilled hole of the gasket between two diamonds and pressed to about 30 GPa with the thickness of 25  $\mu\text{m}$  as an insulating layer. Then a hole of 33  $\mu\text{m}$  in diameter right in the center of the *c*-BN layer was drilled as the sample chamber. The platinum foil with the thickness of 5  $\mu\text{m}$  were pressed on the surface of *c*-BN as presented in Fig. 2-15.

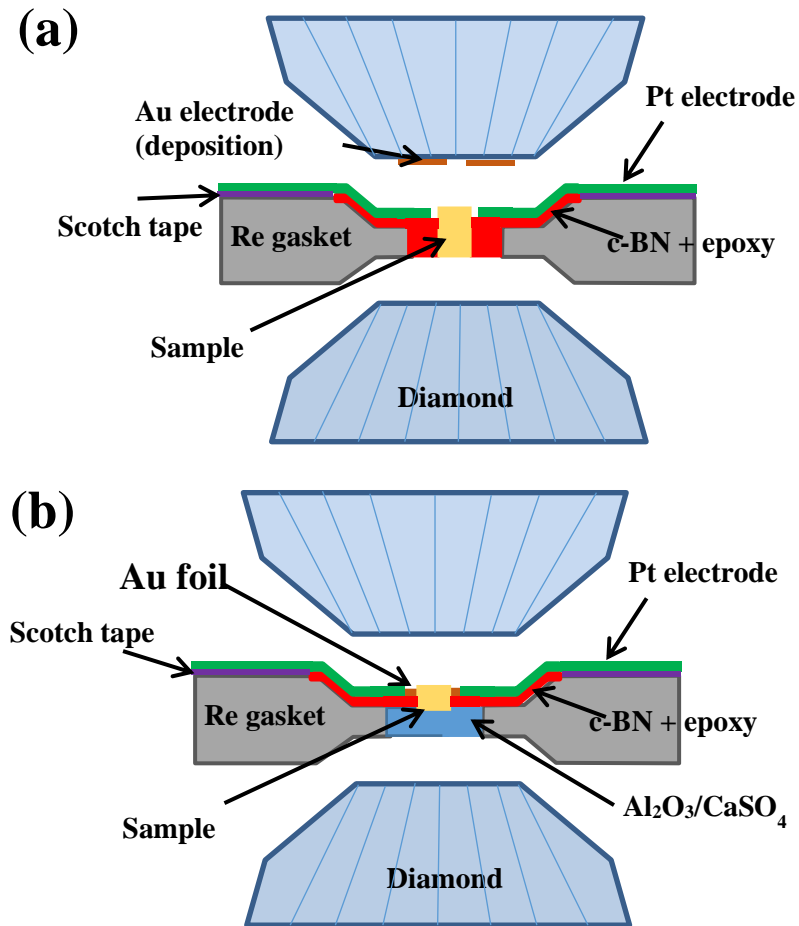


Fig. 2-14 the sketch of the setting method on the gasket (a) and (b).

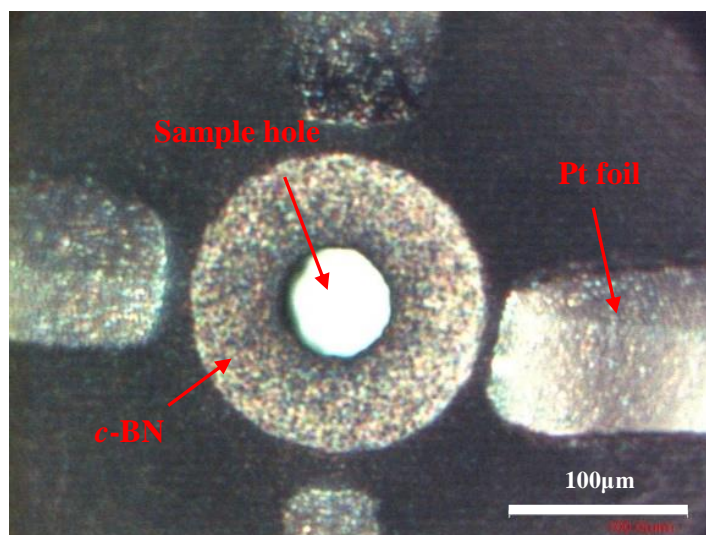


Fig. 2-15 the sample chamber on the gasket.

A proper deposition of the gold film on the culet of diamond with the deposition diameter of 250  $\mu\text{m}$  (when the culet diameter is 100  $\mu\text{m}$ ) was chosen as part of the electrode. The deposition was done in a vacuum arc gun apparatus as shown in Fig. 2-16. The extra deposition films were removed by the UV laser as shown in Fig. 2-17. During the removing of the films, the powder of the laser should to be controlled with a suitable intensity in order to prevent the damage of the diamond. The designed shapes of the electrodes can be seen in Fig. 2-18 (a) and (b). The electrodes on the culet region must connect the platinum electrodes so as to make a circuit. The relative position of the electrodes and the holes on the gasket can be seen in Fig. 2-19 (a) and (b). The white region is the sample hole.

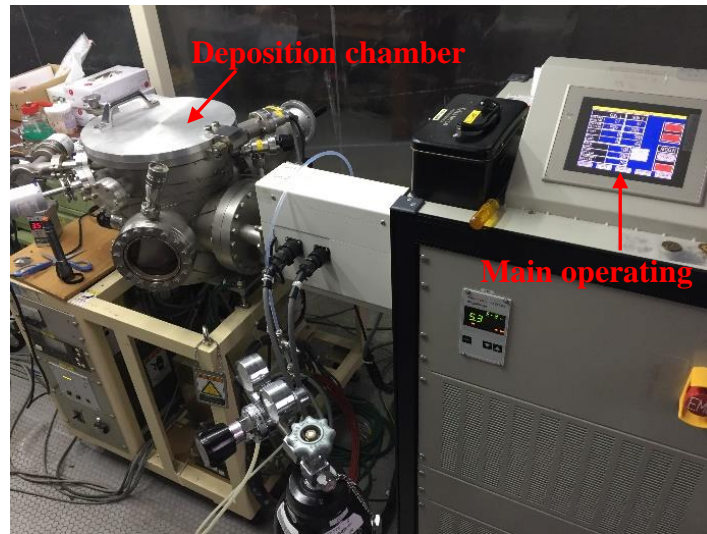


Fig. 2-16 the arc gun deposition apparatus.

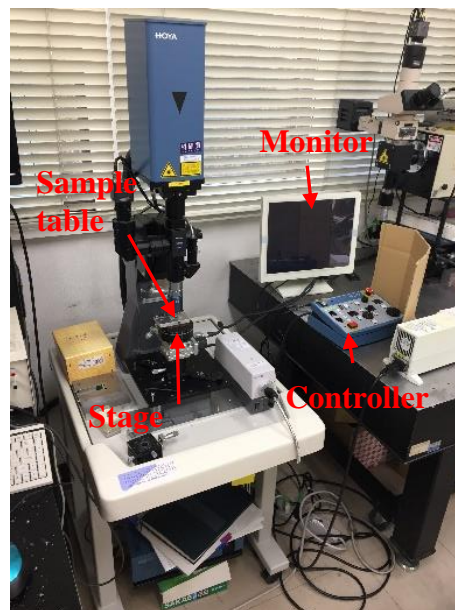


Fig. 2-17 the UV laser for designing the Au electrode.

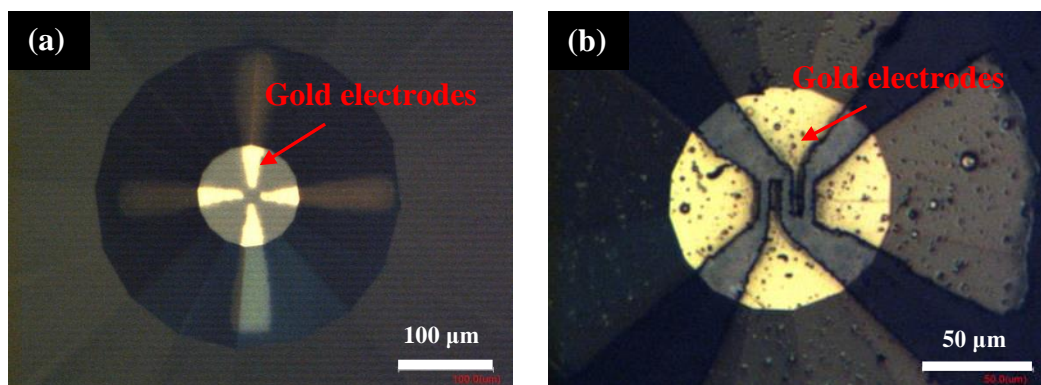


Fig. 2-18 the electrode on the top diamond with different shape in (a) and (b).

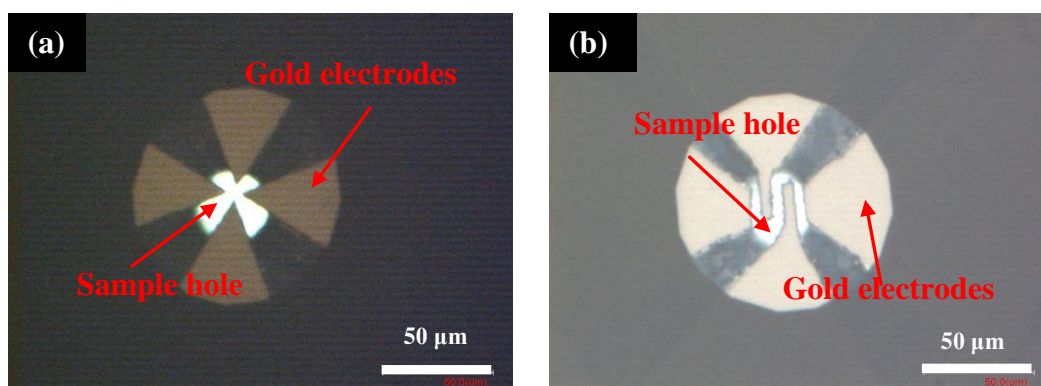


Fig. 2-19 the relative position of the electrodes and the hole after the top diamond approaching to the gasket (a) and (b).

In method 2, the deposition film was replaced by the gold foil with the thickness of 1  $\mu\text{m}$  as the electrode. Furthermore, the  $\text{Al}_2\text{O}_3$  or  $\text{CaSO}_4$  were chosen as the insulating layer due to the transparent property. Thus the color and the outline of the sample can be judged easily. The sketch of this setting method is shown in Fig. 2-14 (b). The relative position of the gold electrodes on the gasket can be seen in Fig. 2-20 (a). One side of the gold foils were on the insulating layer so as to connect the sample and the other side were connected with the Pt foils. After loading the sample in the DAC, the color and the position of the sample is easier to observe through the transmission light (Fig. 2-20b). However, the prone failures of the configuration of the electrodes happened on this method. A perfect position of the electrodes need skill and practice.

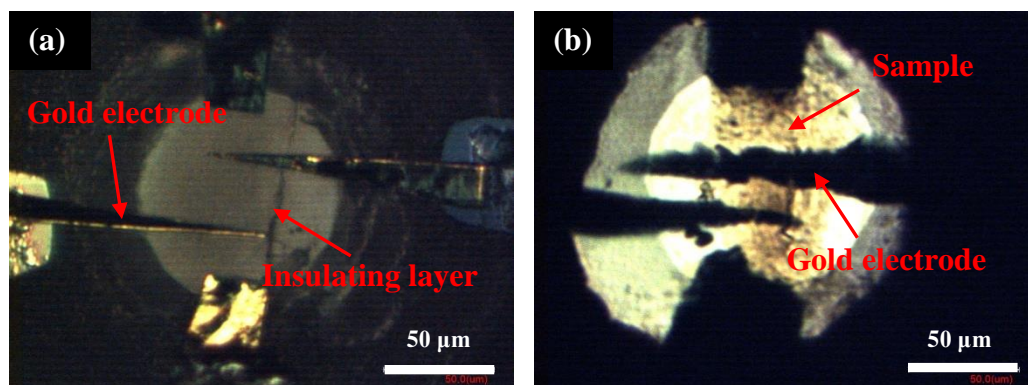


Fig. 2-20 the position of the gold foil on the gasket (a) and the electrode position after loading the sample (b).

In both methods, the platinum foils were put on the surface of Re gasket and insulated by the tape. The copper lead was chosen to connect the platinum foil and the channel as one part of the electrode as shown in Fig. 2-21. The lead was glued on the holder.

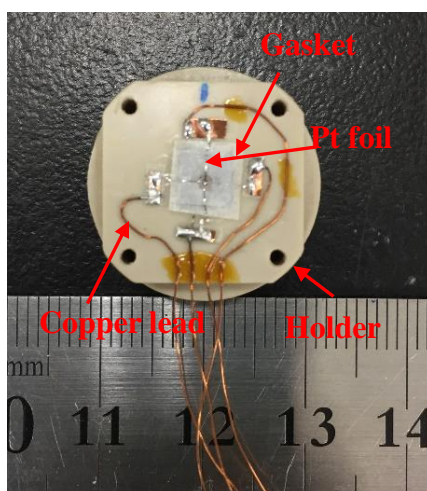


Fig. 2-21 the gasket holder and the lead for electrical resistance measurement.

### 2.3 Sample preparation

The sample was synthesized with the high pressure and high temperature method by Prof. Orimo's group in Tohoku University. The high purity of raw Mo and LiH were mixed with molar ratio of 1:6 for 4 h under 0.1 MPa argon atmosphere. The mixture was compressed into pellets with thickness and diameter of 1.0 mm and encapsulated in the

sample capsules. The capsules and the hydrogen source  $\text{AlH}_3$  were loaded in the NaCl chamber in order to seal the gas source. The NaCl chamber was pressurized to 5 GPa at room temperature and then increase temperature to 973 K for 24 h [14]. The color of the sample is yellow at room temperature as shown in Fig. 2-22. The synthesized samples were characterized after recovery by Raman spectra and XRD. The loading of the sample to the sample chamber conducted in the glovebox due to the high chemical activity of the sample to oxygen and water. In the glovebox, the oxygen and water keep lower than 1 ppm as shown in the Fig. 2-23. The sample was pressed into pieces and loaded into the sample chamber by needle or hair.

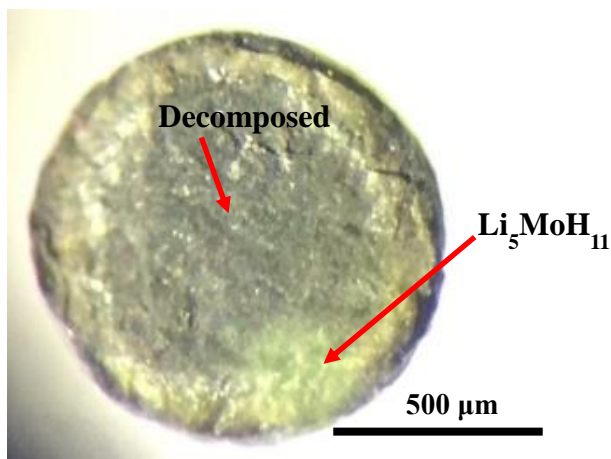


Fig. 2-22 the sample pellet of  $\text{Li}_5\text{MoH}_{11}$ .



Fig. 2-23 the glovebox for loading sample in insert atmosphere.

## 2.4 Pressure determination

Due to the target pressure of 200 GPa, in this experiment the pressures were determined by the diamond anvil Raman method [15]. The first-order Raman spectrum of diamond at ambient pressure is  $1333.1 \text{ cm}^{-1}$ . The high frequency edge of the Raman spectrum observed at the center of the diamond tip face shows a linear relationship correlated with the normal stress at the culet face up to 30 GPa [16]. Up to now, the high frequency edge of the first-order Raman spectrum was calibrated against the EOS scale of Pt up to 310 GPa [15]. The pressure of the diamond at the culet and sample interface is the same as the pressure on the sample. Thus, the Raman spectrum is used to determine the sample pressure. The pressure on the diamond shows the same as the sample pressure in hydrostatic conditions. While the pressure on the diamond would be almost the sample as the sample pressure in non-hydrostatic conditions. The correlation is unique and almost independent of the loading conditions such as culet size and the sample material. The high frequency edge of the diamond often shows different shapes due to the pressure conditions and the sample situation. Thus the definition of the high frequency edge is very important. In this experiment, the high frequency edge of the Raman spectra was defined as the minimum of the differential spectrum  $dI/d\nu$ .

$$P(\text{GPa})=K \frac{\Delta\nu}{\nu} \left[ \mathbf{1} + \frac{1}{2} (K' - \mathbf{1}) \frac{\Delta\nu}{\nu} \right] \quad (11)$$

Where P is pressure, K is a bulk modulus and K' is its pressure derivative.  $\nu$  is the edge of Raman spectrum at ambient pressure and  $\Delta\nu$  is the edge at calibrated pressure. The bulk modulus of  $K=547$  (11) GPa and the pressure derivative of the bulk modulus  $K'=3.75$  (20) were determined. Fig. 2-24 (a) and (b) shows the Raman spectrum of diamond at ambient pressure and high pressure, respectively.

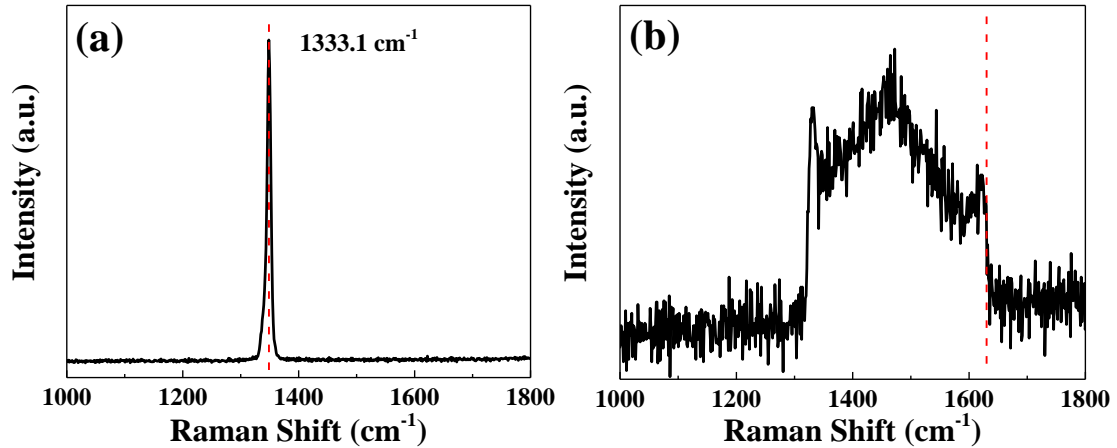


Fig. 2-24 the diamond Raman spectra at ambient pressure (a) and high pressure (b).

## 2.5 High pressure measurements of DACs

The high range resistance measurements were carried out at Keithley Model 6517 High Resistance Meter, which can provide the basic procedure to perform the resistance measurement and the configuration information. The pressure dependence of resistance relationship of the sample was measured in AC four-terminal-measurement mode with Model 370 AC resistance Bridge, LakeShore Cryotronics, Inc. The resistance measurement ranges from 2 m $\Omega$  to 2 M $\Omega$  and the excitation levels varies from 3.16 pA to 31.6 mA. This apparatus combines with a full range of design strategies which optimize resolution and minimize measurement uncertainty in low powder resistance measurement. Four leads AC measurement for the best possible accuracy with the lowest possible excitation current.

The cooling of the sample was measured by using liquid helium and <sup>3</sup>He/<sup>4</sup>He dilution refrigerator called Variable Temperature Insert (VTI) system, Oxford Instrument. The temperature of the sample can be controlled by the VTI system continuously over a wide range. Inside the outer vacuum chamber of the cryostat is the sample chamber. The sample is fixed on a top loading probe and cooling by the following helium gas. The sample temperature can typically be controlled from 1.5 K to 300 K by balancing the temperature controller with a heater or the cooling speed of flowing liquid helium. The liquid helium is pumped from the main reservoir and passes through a needle valve, which can be adjusted manually to control the flowing speed. The heater and the control thermometer can be fixed

on the DAC or on the heater exchanger. Thus, the temperature of the sample can be represented by the thermometer on the DAC. By reducing the vapor pressure of the liquid helium in the sample space, the temperature can be cooled below 4.2 K. The liquid helium can fill the sample chamber continuously by set the needle valve. By controlling the flow rate correctly, the flow helium can just replace the evaporating liquid helium and maintain a constant liquid level. Thus, the temperature can be controlled at 1.5 K with this continuously filling. The temperature lower than 1.5 K can be obtained for limited time. When the temperature reaches 1.5 K, then the liquid helium fills the sample space and closed the needle valve completely. By pumping the helium with the largest model to reduce the vapor pressure of the liquid helium, the liquid and the sample usually can be cool down to 1.2 K until all the liquid has evaporated. Fig.2-25 shows the VTI system.

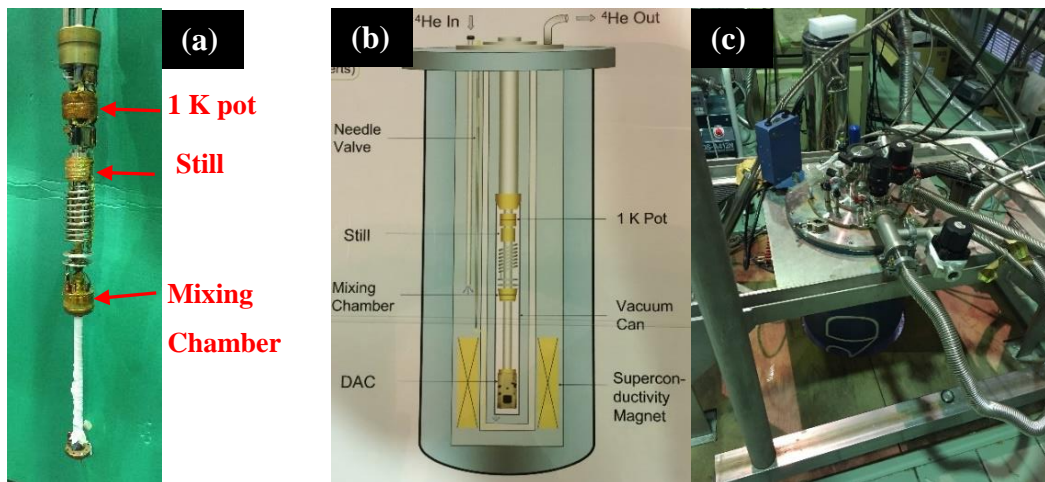


Fig. 2-25 the Variable Temperature Insert (VTI) system.

The temperature below 1.2 K is achieved by the dilution of helium-3 with liquid helium-4 method. This cooling process method was first proposed by H. London and realized by the scientists in Leiden University in 1964 [17]. When the mixture of helium-3 and helium-4 were cooled down to 0.87 K, the mixture experience spontaneous phase separation to form helium-3 rich phase and helium-3 poor phase [18]. The helium-3 gas is pre-cooled by the liquid helium-4 to 4.2 K and further cooled to 1.2-1.5 K by the 1 K pot, which is a helium-4 reservoir with the temperature down to approximately 1 K by decreasing the vapor pressure of helium-4 to depress the boiling point.

The synchrotron powder XRD under high pressure was conducted in the SPring-8 beamline BL10XU as shown in Fig. 2-26. The beamline BL10XU at SPring-8 has been engaged in the powder XRD under high pressure in DACs since 2003 [20]. The high intensity, high energy and quasi-monochromatic synchrotron radiation beam is based on a short period hybrid in-vacuum type undulator. In order to collect high quality XRD data, the high-resolution monochromatic angle-dispersive XRD method is equipped in BL10XU. The XRD experiment can be performed at low temperature down to 10 K with the help of cryostat and high temperature to 4000 K with a laser heating system. The monochromatic and focused X-ray beam ranging from 16 keV to 61 keV can irradiate the sample inside of the DAC up to 300 GPa. A flat imaging plate (IP, Rigaku. Co., R-AXIS IV++;  $300 \times 300$  mm<sup>2</sup>; pixel size 0.1mm) for high statistics measurement and a flat panel detector (FPD, XRD0822 CP23;  $1024 \times 1024$  pixels; 0.2 mm pixel pitch) for rapid recording of the diffraction data were equipped on the diffractometer. The IP is laid on individual automatic linear slide stage in order to vary the camera distance ranging from 150-450 mm. A microscope was used to adjust the position of the DAC to the X-ray beam and observe the sample images inside the DAC. The schematic layout of the experiment setup for the high pressure experiment is shown in Fig. 2-27. In this experiment, the beams were monochromatized to a wavelength of 0.41499 Å and collimated to a diameter of 10 μm. The XRD signals were collected by imaging plate X-ray area detector system.

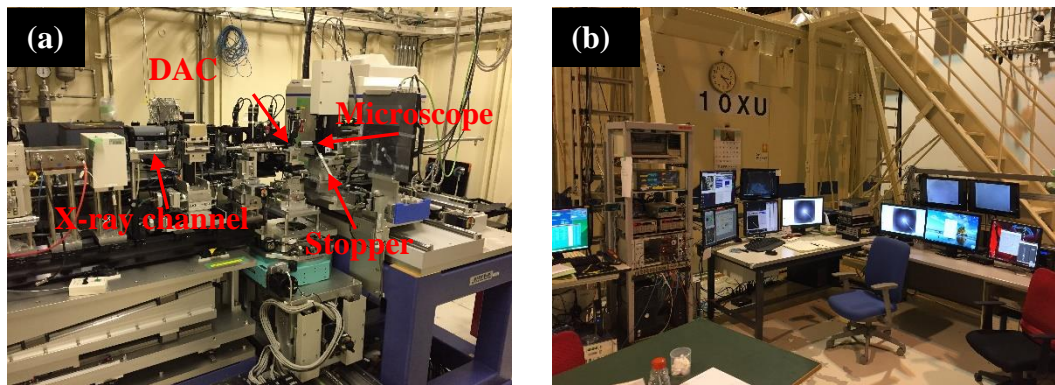


Fig. 2-26 the synchrotron XRD apparatus in BL10XU of SPring-8.

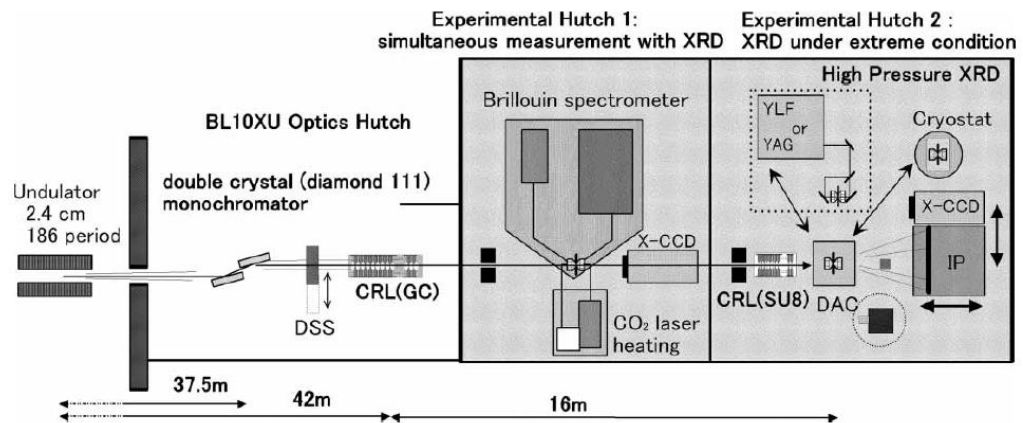


Fig. 2-27 the schematic layout of the experimental setup in BL10XU of Spring-8 [20].

## Reference:

- [1] G. Shen, H.K. Mao, High-pressure studies with x-rays using diamond anvil cells, *Rep. Prog. Phys.*, 80 (2017) 016101.
- [2] W.A. Bassett, Diamond anvil cell, 50th birthday. *High Press Res.*, 29 (2009)163-186.
- [3] B. Li, C. Ji, W. Yang, J. Wang, K. Yang, R. Xu, W. Liu, Z. Cai, J. Chen, H. Mao, Diamond anvil cell behavior up to 4 Mbar, *Proc. Natl. Acad. Sci.*, (2018) 201721425.
- [4] H.K. Mao, P.M. Bell, High-pressure physics: sustained static generation of 1.36 to 1.72 Megabars, *Science*, (1978) 1145-1147.
- [5] R.J. Hemley, H.K. Mao, G. Shen, J. Badro, P. Gillet, M. Hanfland, D. Häusermann, X-ray imaging of stress and strain of diamond, iron, and tungsten at Megabar pressures, *Science*, 276 (1997) 1242-1245.
- [6] Y. Nakamoto, H. Sumiya, T. Matsuoka, K. Shimizu, T. Irifune, Y. Ohishi, Generation of multi-megabar pressure using nano-polycrystalline diamond anvils, *Jpn. J. Appl. Phys.*, 46 (2007) L640-L641.
- [7] K. Shimizu, New superconductors under very high pressure, *J. Phys. Condens. Matter*, 19 (2007) 125207.
- [8] I. Kantor, V. Prakapenka, A. Kantor, P. Dera, A. Kurnosov, S. Sinogeikin, N. Dubrovinskaia, L. Dubrovinsky, BX90: A new diamond anvil cell design for X-ray diffraction and optical measurements, *Rev. Sci. Instrum.*, 83 (2012) 125102.
- [9] R. Boehler, New diamond cell for single-crystal x-ray diffraction, *Rev. Sci. Instrum.*, 77 (2006) 115103.
- [10] W.A. Bassett, T. Takahashi, P.W. Stook, X-ray diffraction and optical observations on crystalline solids up to 300 kbar, *Rev. Sci. Instrum.*, 38 (1967) 37-42.
- [11] G.J. Piermarini, S. Block, Ultrahigh pressure diamond-anvil cell and several semiconductor phase transition pressures in relation to the fixed point pressure scale, *Rev. Sci. Instrum.*, 46 (1975) 973-979.
- [12] Y. Liu, J. Wang, M. Azuma, W.L. Mao, W. Yang, Five-dimensional visualization of phase transition in  $\text{BiNiO}_3$  under high pressure, *Appl. Phys. Lett.*, 104 (2014) 043108.
- [13] H.K. Mao, J. Shu, G. Shen, R.J. Hemley, B. Li, A.K. Singh, Elasticity and rheology of iron above 220 GPa and the nature of the Earth's inner core, *Nature*, 396 (1998) 741-743.

- [14] S. Takagi, Y. Iijima, T. Sato, H. Saitoh, K. Ikeda, T. Otomo, K. Miwa, T. Ikeshoji, S. Orimo, Formation of novel transition metal hydride complexes with ninefold hydrogen coordination, *Sci. Rep.*, 7 (2017) 44253.
- [15] Y. Akahama, H. Kawamura, Pressure calibration of diamond anvil Raman gauge to 310 GPa, *J. Appl. Phys.*, 100 (2006) 043516.
- [16] M. Hanfland, K. Syassen, A Raman study of diamond anvils under stress, *J. Appl. Phys.*, 57 (1985) 2752-2756.
- [17] H. London. *Proc. Internat. Conf. Low Temperature Physics*, Clarendon, Oxford, 1951:157.
- [18] P. Das, R. de Bruyn Ouboter, and K. W. Taconis, A Realization of a London-Clarke-Mendoza Type Refrigerator, *Low Temperature Physics*, LT9, 1965:1253-1255.
- [19] C. Enss, S. Hunklinger, *Low-temperature physics*, Springer, 2005:139.
- [20] Y. Ohishi, N. Hirao, N. Sata, K. Hirose, M. Takata, Highly intense monochromatic X-ray diffraction facility for high-pressure research at SPring-8, *High Press. Res.*, 28 (2008) 163-173.

# Chapter 3. Superconductivity of $\text{Li}_5\text{MoH}_{11}$ under high pressure

In this chapter, the results of the superconducting behavior of  $\text{Li}_5\text{MoH}_{11}$  under the effect of pressure will be presented. Two separate runs will show the pressure dependence of resistance, the effect of magnetic field on the temperature dependence of resistance curves, the phase diagram of pressure versus temperature. Then the synchrotron powder XRD will exhibit the crystal structure of the sample under pressure. At last the discussion part will exhibit the comparison of the results in depth.

## 3.1 Introduction of $\text{Li}_5\text{MoH}_{11}$

Transition metal could combine hydrogen atoms to form the hydrogen-rich hydrides. In these hydrides, the transition metals are surrounded by the hydrogen atoms from two-fold to nine-fold such as  $\text{MgFeH}_6$ ,  $\text{Mg}_3\text{CrH}_8$ ,  $\text{BaReH}_9$  and  $\text{Li}_5\text{MoH}_{11}$  [1-4]. Most of these hydrides have already synthesized under high pressure and high temperature conditions, which are different from metal hydrides  $\text{CaH}_6$  or  $\text{YH}_{10}$  that only predicted in theory.

One of the hydrides  $\text{BaReH}_9$  with  $\text{ReH}_9$  unit shows superconductivity at around 100 GPa with  $T_c$  of 7 K [5]. The high hydrogen coordination in  $\text{ReH}_9$  unit shows hydrogen density twice than that of liquid hydrogen at ambient pressure. Among these transition metal hydrides,  $\text{Li}_5\text{MoH}_{11}$  contains the highest hydrogen coordination numbers of 11 in all the ternary hydrides. Thus, in this study the transition metal hydride  $\text{Li}_5\text{MoH}_{11}$  is focused. In  $\text{Li}_5\text{MoH}_{11}$ , the crystal structure is hexagonal and the Mo is surrounded by nine hydrogen atoms with a tricapped trigonal prism which is confirmed by the neutron diffraction [4]. Fig. 3-1 (a) and (b) shows the crystal structure of  $\text{Li}_5\text{MoH}_{11}$  and  $\text{Li}_5\text{MoD}_{11}$ , respectively. The  $\text{Li}_5\text{MoH}_{11}$  hydride presents the  $P6_3cm$  (No. 185) space group of hexagonal structure while the  $\text{Li}_5\text{MoD}_{11}$  deuteride displays the hexagonal structure of space group  $P6cc$  (No. 184). According to the calculation of the density of states, the band gap of  $\text{Li}_5\text{MoH}_{11}$  at ambient pressure is 4.0 eV as shown in Fig. 3-2. The hydrogen 1s states which reach the Fermi level strongly hybridized with the Mo *spd* states to form the  $\sigma$ -bonds. The possible

strong electron-phonon coupling may be expected if the band gap is closed by the applying of pressure.

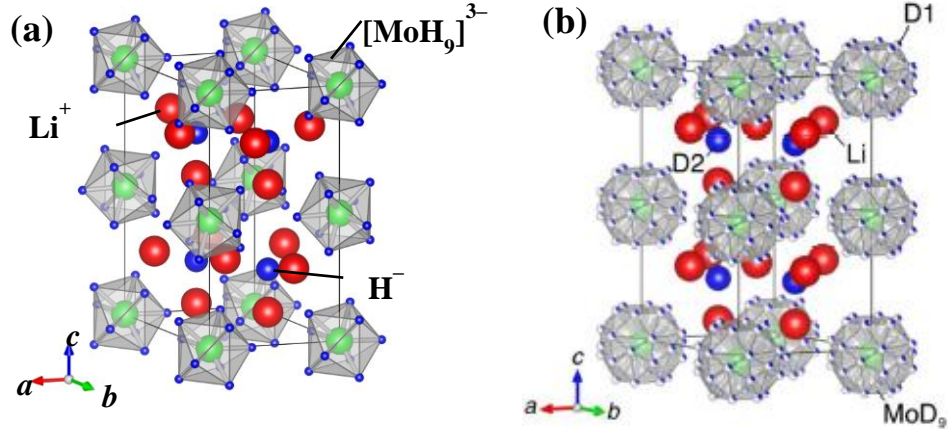


Fig. 3-1 the crystal structure of  $\text{Li}_5\text{MoH}_{11}$  (a) and  $\text{Li}_5\text{MoD}_{11}$  (b).

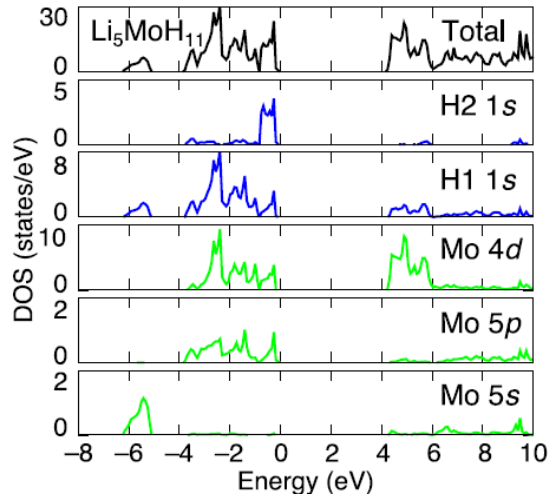


Fig. 3-2 the density of states of  $\text{Li}_5\text{MoH}_{11}$ .

Furthermore, in the theoretical calculation two possible phase transitions may happen under the effect of high pressure. The first phase transition happens at 5 GPa with the structure from  $P6_3cm$  to monoclinic  $Cc$ , which shows insulating behavior by the electronic structure calculation. Then, with the increase of pressure, the second phase transition occurs at 94 GPa from monoclinic  $Cc$  to monoclinic  $Pc$  structure as presented in Fig. 3-3. Furthermore, the redistribution of the hydrogen sublattice induces the metallic behavior,

which happens between 85 GPa and 94 GPa. A more hydrogen-rich unit of  $\text{MoH}_{11}$  may form in this phase transition. Thus, it is quite interesting to explore the effect of pressure on the electrical properties and structural phase transition of  $\text{Li}_5\text{MoH}_{11}$ .

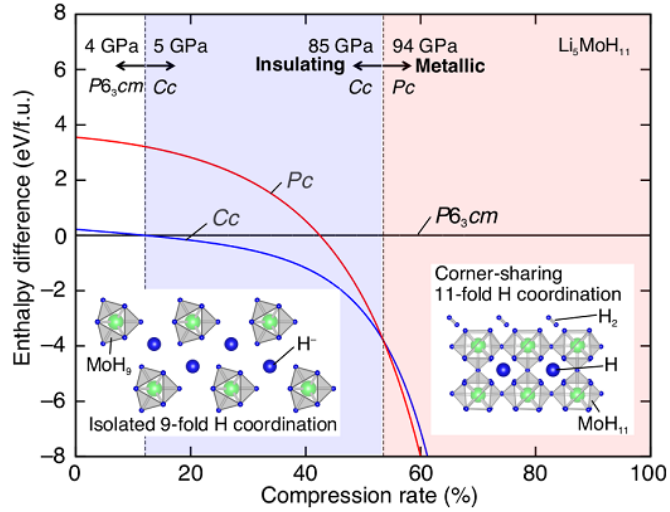


Fig. 3-3 the thermodynamic stability of three competing phases of  $\text{Li}_5\text{MoH}_{11}$  as a function of compression rate.

### 3.2 The result of long time annealing

Fig. 3-4 (a) shows the sample in the DAC after loading under the pressure of 6 GPa. It is difficult to judge the outline of the sample since the insulating layer  $c\text{-BN}$  is not transparent at this pressure. When the pressure increased to 40 GPa, the outline of the sample with black color was clear to see as shown in Fig. 3-4 (b)

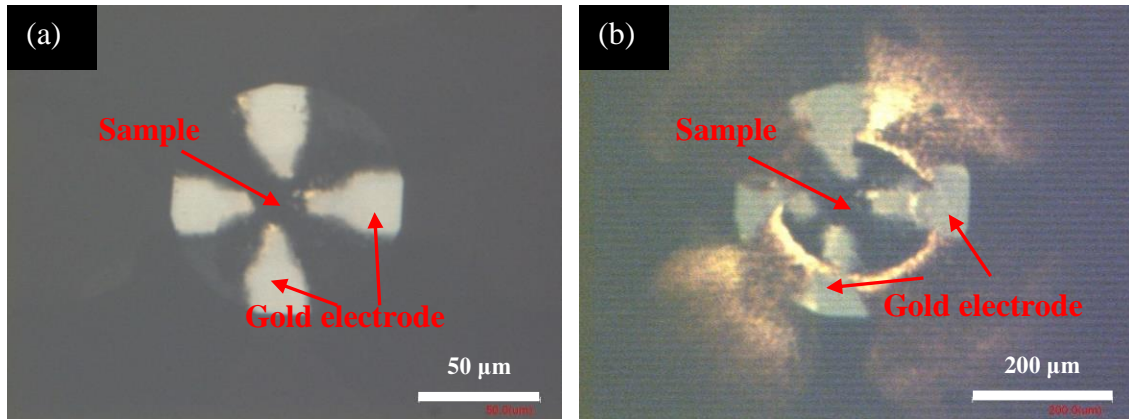


Fig. 3-4 the photograph of the sample in the DAC under 6 GPa (a) and 40 GPa (b).

### 3.2.1 The temperature dependence of electrical resistance under pressure

$\text{Li}_5\text{MoH}_{11}$  is an insulator at ambient pressure. The electrical resistance measurements are conducted as functions of pressure and temperature to explore the pressure effects on the conducting behavior. During pressurization at room temperature, the resistance undergoes a drop by two orders of magnitude until 100 GPa as shown in Fig. 1a. The resistance is saturated above 100 GPa with the resistivity of around  $0.001 \Omega \cdot \text{cm}$ , where the corresponding conductivity ( $1000 \Omega^{-1} \cdot \text{cm}^{-1}$ ) is close to the minimum conductivity of metal [31, 32]. Thus,  $\text{Li}_5\text{MoH}_{11}$  transforms from an insulator to a poor metal at room temperature under the pressure above 100 GPa.

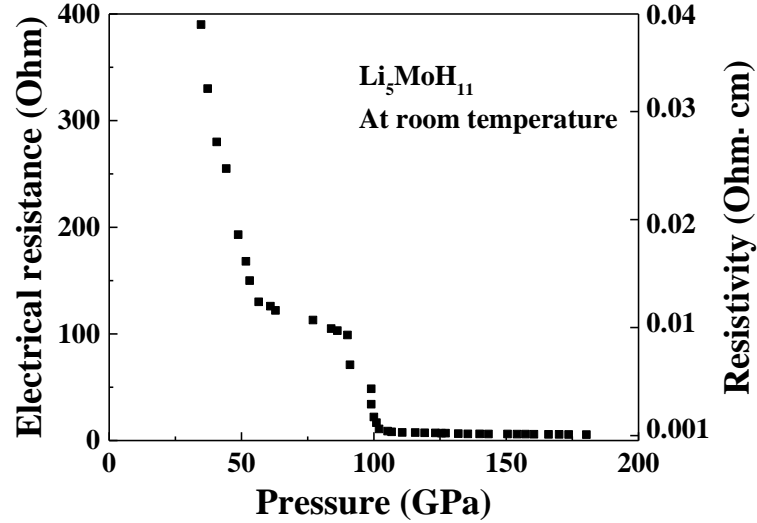


Fig. 3-5 the pressure dependence of electrical resistance at room temperature.

The conducting behavior of the sample can be obtained in the temperature dependence of electrical resistance curves. The electrical resistance-temperature ( $R$ - $T$ ) curve at 77 GPa is shown in Fig. 3-6. The pressure was measured at room temperature. It was seen from the curve that the sample showed insulating behavior. Usually, the pressure would increase with the cooling of the DAC due to the shrinkage of the piston and nut. On the other hand, the pressure shows drop tendency during the heating process. The added value of pressure changes after cooling is larger than the reduced value after heating. Thus, after one circle of the cooling process, the pressure of the diamond usually increases. Fig. 3-7 shows the temperature dependence of pressure from 300 K to 10 K. The starting pressure was 103 GPa at room temperature and increased to 112 GPa at 10 K, then decreased to 106 GPa after heating to room temperature. In the cooling process, the changes of pressure can affect the conducting behavior. The value of resistance is derived from the competing of pressure effect and temperature effect. The sample shows insulating behavior at heating process. This conducting behavior is the combination of decompression and heating temperature. In this sample, the pressurization lead to the decrease of resistance. Thus, during decompression process the resistance decrease, which is the same behavior of the increased temperature on the effect of insulating materials. Finally, the sample shows insulating behavior.

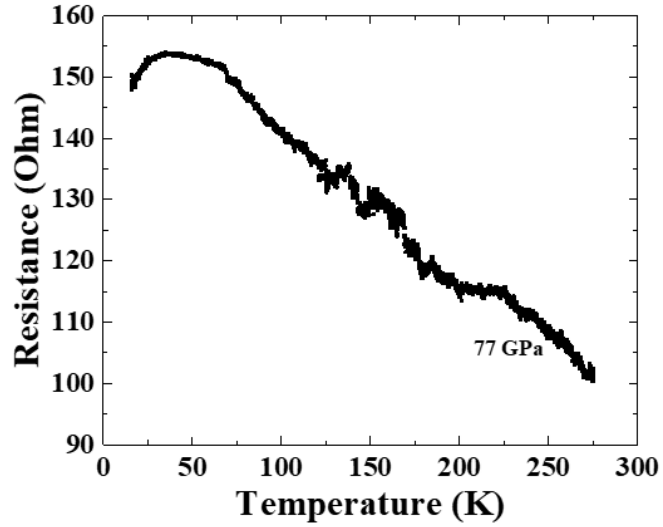


Fig. 3-6 the temperature dependence of resistance at 77 GPa.

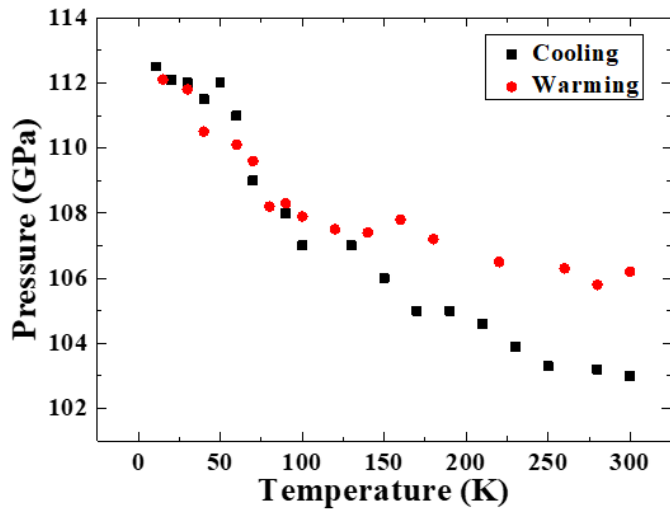


Fig. 3-7 the pressure varieties as a function of temperature.

Intriguingly, the sample showed metallic behavior after 48 days room temperature annealing at 77 GPa as can be seen in Fig. 3-8. The negative slopes of the  $dR/dT$  became positive. The result indicated the time lag phenomenon on the sample. The transition metal hydride BaReH<sub>9</sub> also showed the time dependence behavior, which induced the insulating to metallic behavior transformation [1].

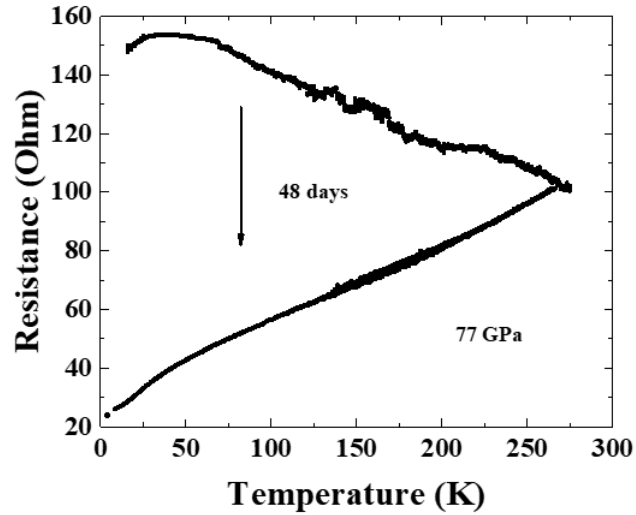


Fig. 3-8 the temperature dependence of resistance at 77 GPa. The sample shows the metallic behavior after room temperature annealing for 48 days at 77 GPa.

In further increasing the pressure, the sample again exhibited insulating behavior at 90 GPa before cooling and 100 GPa after heating to room temperature as shown in Fig. 3-9. The sample shows time dependence behavior at 100 GPa room temperature. The resistance decreased from 48  $\Omega$  to 10  $\Omega$  after 35 days room temperature annealing at 100 GPa. Furthermore, the temperature dependence of resistance ( $R$ - $T$ ) relationships were also examined. The results illustrate that the sample presents insulating behavior and the slopes of  $dR/dT$  in the  $R$ - $T$  curves decrease with annealing time, which suggests the insulating behavior is suppressed with the time of duration.

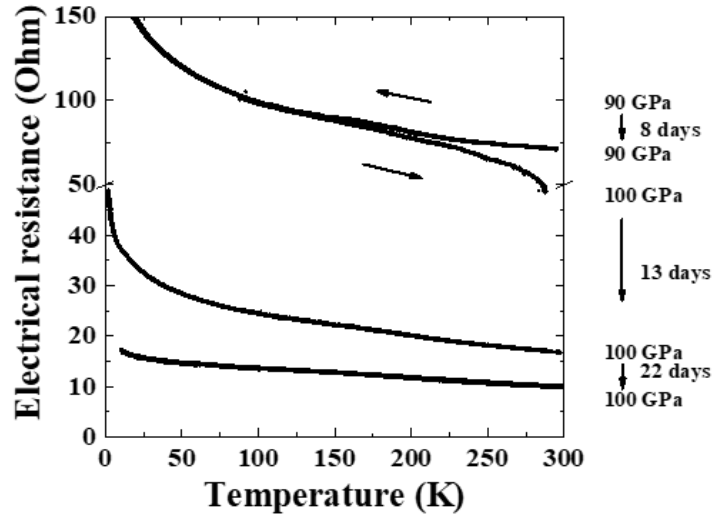


Fig. 3-9 the temperature dependence of resistance at 90-100 GPa.

At 120 GPa, a peak was observed on the  $R$ - $T$  curve, which reached the maximum resistance at 21 K as shown in Fig.3-10 (a). The insulating behavior was suppressed by the increase of pressure. Thus, the metallic behavior appeared. Since the time lag may have an effect on the conducting behavior, the temperature dependence of resistance as a function of annealing time at 120 GPa was conducted (Fig. 3-10b). The temperature where the resistance reaches the maximum shifted to higher temperature with the annealing time. Furthermore, when the low temperature regions were checked as shown in Fig. 3-10 (c), the metallic behavior was obvious with the annealing time. All regions below 14 K showed metallic behavior from 64 days annealing. An obvious drop of resistance was caught after 270 days annealing compared with 231 days annealing.

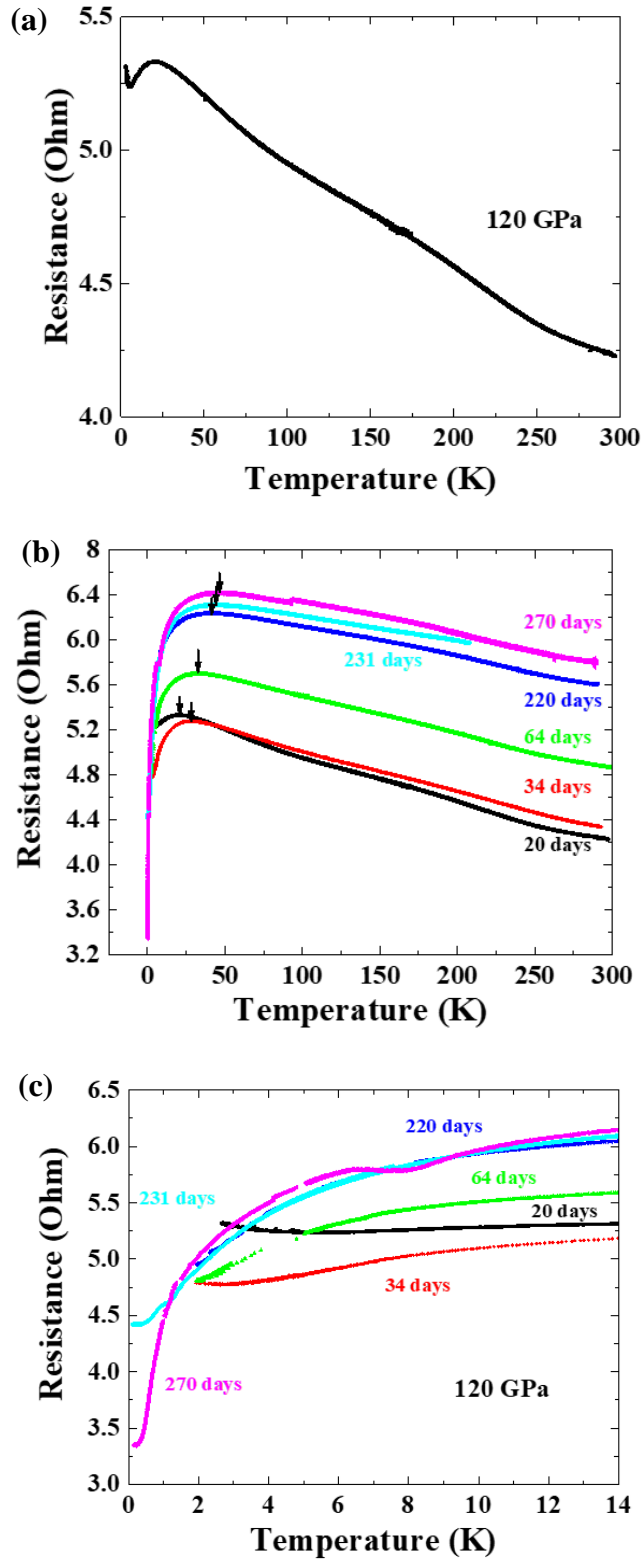


Fig. 3-10 the temperature dependence of resistance at 120 GPa: (a) 20 days room temperature annealing; with different annealing time at 0-300 K (b) and 0-14 K (c).

With the pressurization, totally the resistance decreases with the increase of pressure. Fig. 3-11 presents the temperature dependence of resistance from 130 GPa to 170 GPa, the highest pressure of this run. Up to 170 GPa, zero resistance cannot be detected when the sample was cooled below 0.1 K. The reason can be explained by the extra resistance of lead and channel between the sample and the tester. A flat tendency of resistance changes with constant value can be observed below 0.5 K at 140 GPa and 148 GPa. It suggests that the superconducting transition have already finished with the cooling of temperature down to 0.5 K. The drop of resistance in the  $R$ - $T$  curve became obvious with the increase of pressure, which exhibits the drop of resistance rate exceeding more than 20 % at 130 GPa as shown in Fig. 3-12. What's more, the percentage of the resistance drop became promising, showing more than 90 % of resistance loss at 170 GPa. The loss resistance rate increase with the growing of pressure, which illustrates that the pressure have a positive effect on the transition of superconducting behavior.

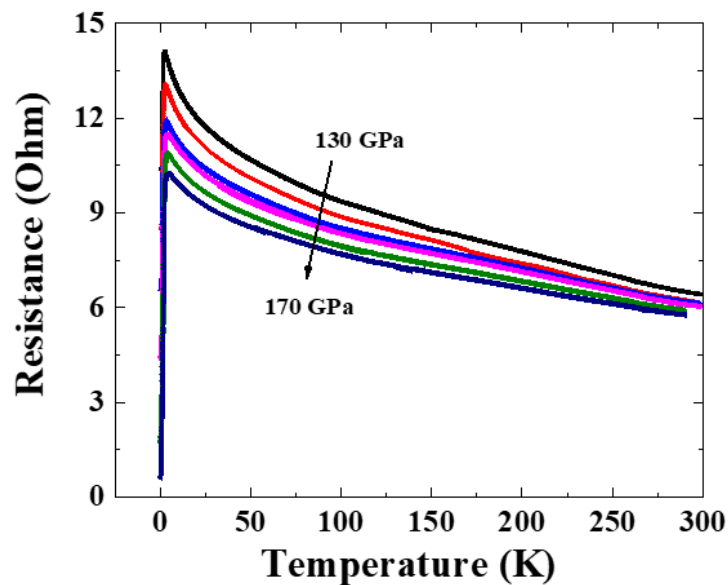


Fig. 3-11 the temperature dependence of resistance at different pressures.

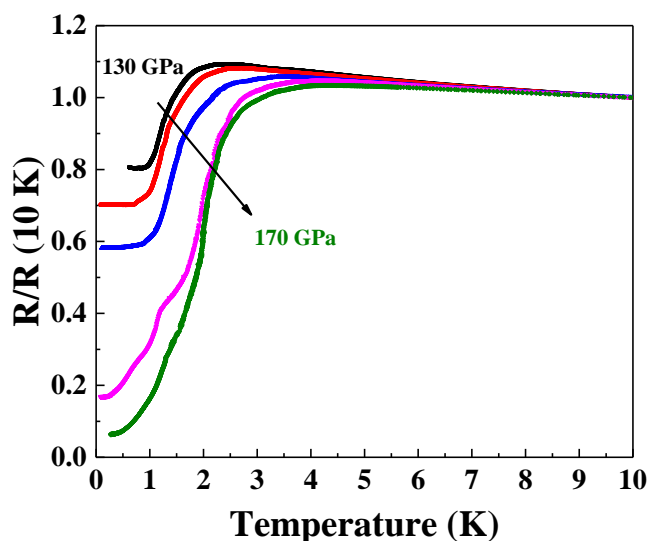


Fig. 3-12 the temperature dependence of resistance at 130-170 GPa normalized at 10 K.

Since the sample showed time dependence behavior, the experimental period is very long. Fig. 3-13 list the consuming time with the changes of pressure and room temperature resistance of the sample. Sufficient annealing time was used to stabilize the resistance and  $R$ - $T$  curves. The insulating behavior transformed to metallic behavior with the time dependence behavior.

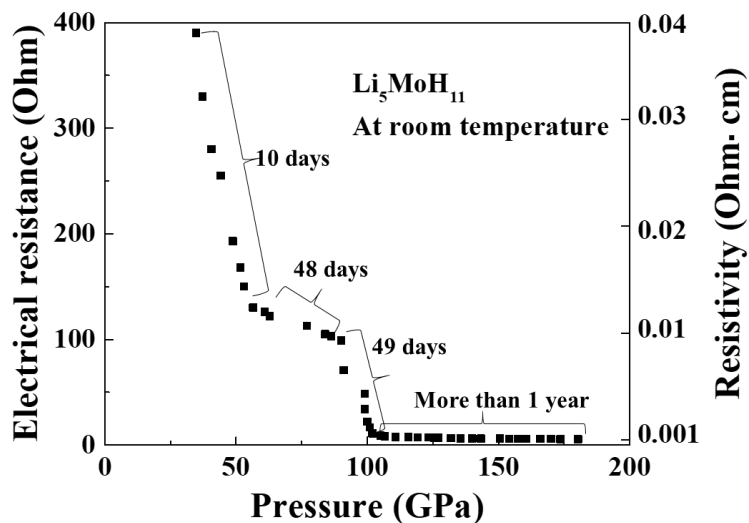


Fig. 3-13 the pressure dependence of resistance at room temperature with long experimental period of more than one and a half years.

### 3.2.2 The effect of magnetic field on the temperature dependence of resistance

In order to confirm the drop of resistance resulting from the superconducting transition, the temperature dependence of resistance curves as a function of the magnetic field were carried out. At 120 GPa annealing 270 days, with the applying of the magnetic field the deviation of the resistance was observed at 3.0 K, which indicated the appearance of superconductivity as shown in Fig. 3-14.

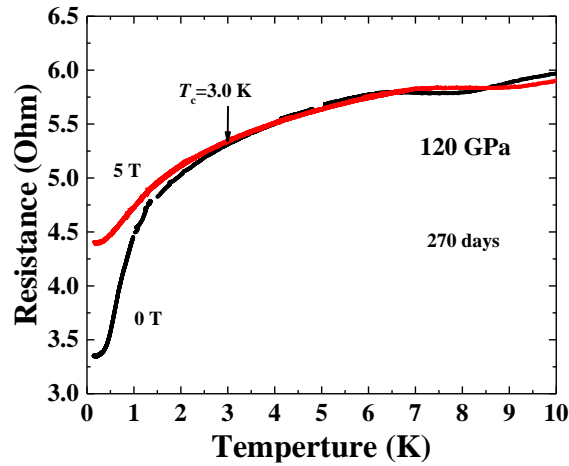


Fig. 3-14 the temperature dependence of resistance at 120 GPa after annealing 270 days with the effect of magnetic field of 5 T at low temperature region.

When the incremental magnetic fields applied to the sample at 140 GPa, the suppression of the resistance drop became obvious. No drop of resistance was observed in the magnetic field of 4 T when the sample cooling down to 1K as shown in Fig. 3-15. To further understand this behavior, the relationship between upper critical field and onset transition temperature was plotted in Fig. 3-16. The upper critical field  $H_{c2}$  at zero can be calculated by Werthamer-Helfand-Hohenberg formula  $H_{c2}(0) = -0.693T_c (dH_{c2}/dT)_{T=T_c}$  [3]. The dashed line represents the temperature dependence of calculated  $H_{c2}$ . The calculated  $H_{c2}$  result at zero Kelvin 4.2 T is coincident with the experimental result that 4 T can restrain

the superconductivity. The high value of the  $H_{c2}$  signifies this new superconductor belongs to the type II superconductor. There is no obvious change of the  $R$ - $T$  curve at 130 GPa in various times up to 18 days. It means that the time dependence cannot affect the superconducting phase after the sample shows superconductivity. The zero resistance cannot be observed may result from the deformation resistance due to the extrusion under high pressure.

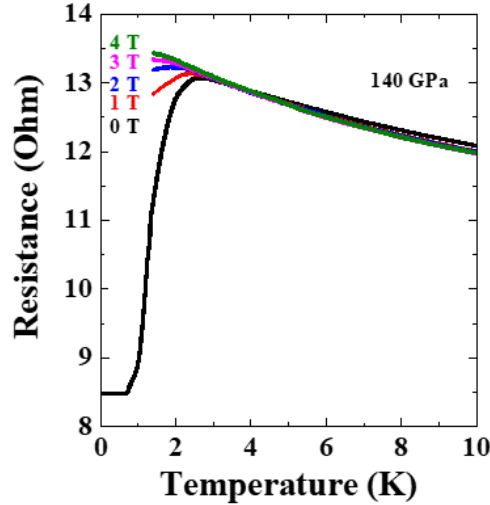


Fig. 3-15 the temperature dependence of resistance at 140 GPa with the effect of magnetic fields from 0 T to 4 T at low temperature region.

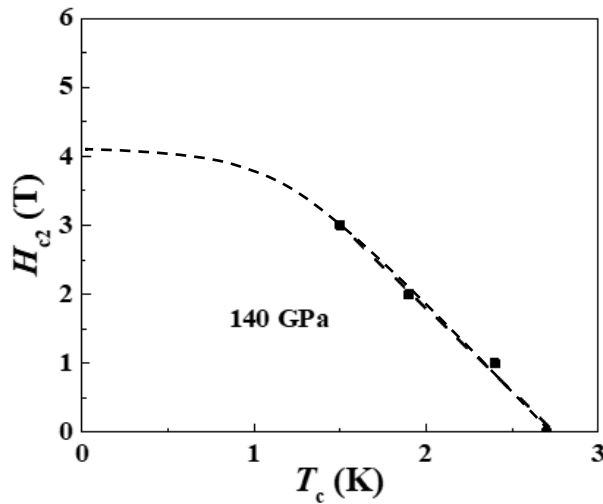


Fig. 3-16 Upper critical field  $H_{c2}$  for the pressure of 140 GPa.  $T_c$  was determined from the onset of resistance drop. The dashed line comes from the calculated  $H_{c2}$  based on the Werthamer-Helfand-Hohenberg formula.

### 3.2.3 The diagram of pressure versus temperature

The definition of  $T_c$  is the deviation of the resistance curves from the linear temperature dependence as described in Fig. 3-17, which shows the  $T_c$  of 2.75 K at 140 GPa. In order to understand the changes of the  $T_c$  with the effect of pressure, the pressure dependence of temperature diagram is shown in Fig. 3-18. The insulating behavior to metallic behavior transition happens at around 100 GPa. The superconducting behavior appeared at 120 GPa with  $T_c$  of 3.0 K and the  $T_c$  grows to 4.3 K at 170 GPa, the highest pressure of this experiment.

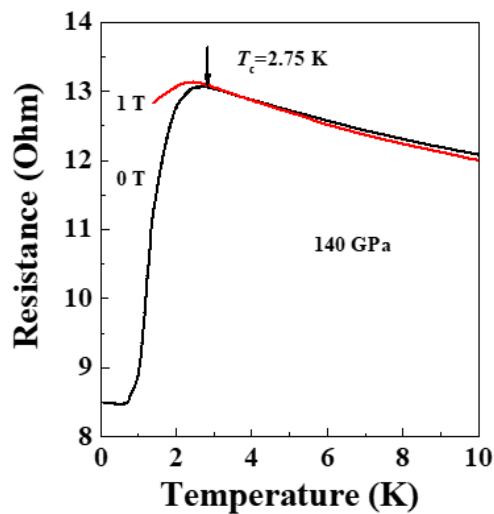


Fig. 3-17 the definition of  $T_c$  as the deviation of the resistance curves from the linear temperature dependence.

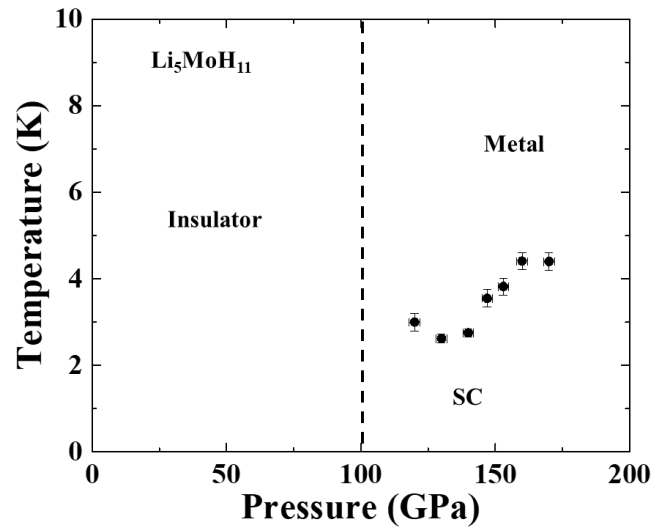


Fig. 3-18 the pressure dependence of  $T_c$ .

### 3.3 Results of short time annealing

In previous research, we found the resistance changes with the time dependence behavior, which result in a long experimental period. In this time, a relative short room temperature annealing time was chosen to investigate the metallization and superconductivity of  $\text{Li}_5\text{MoH}_{11}$ .

Fig. 3-19 represents the sample inside the DAC under 40 GPa. The sample can be seen combining the transmission light and reflected light, which shows black color and connects with the four electrodes.

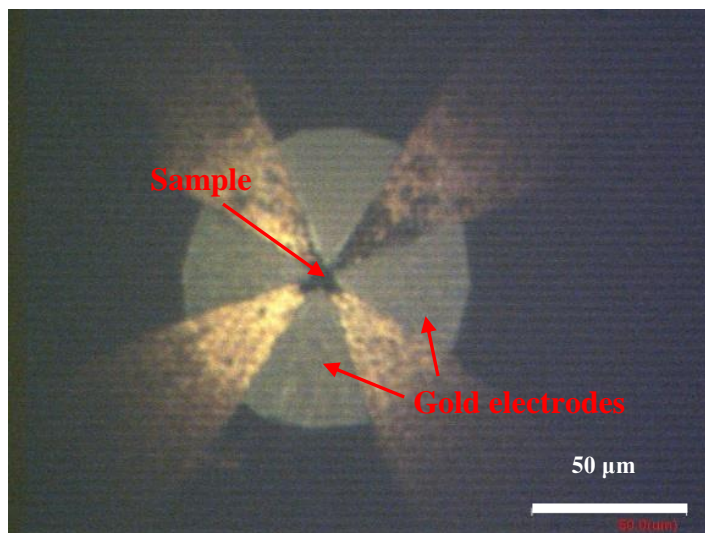


Fig. 3-19 the sample in the DAC under 40 GPa.

### 3.3.1 The temperature dependence of electrical resistance under pressure

The pressure dependence of electrical resistance at room temperature is shown in Fig. 3-20. The resistance decreased with the increase of pressure continuously by two orders of magnitude from 5 kΩ at 13 GPa to 30 Ω at 90 GPa. The changes tendency of the resistance with the effect of pressure shows similar with last run. The discrepancy may come from the connect area of the sample and the annealing time.

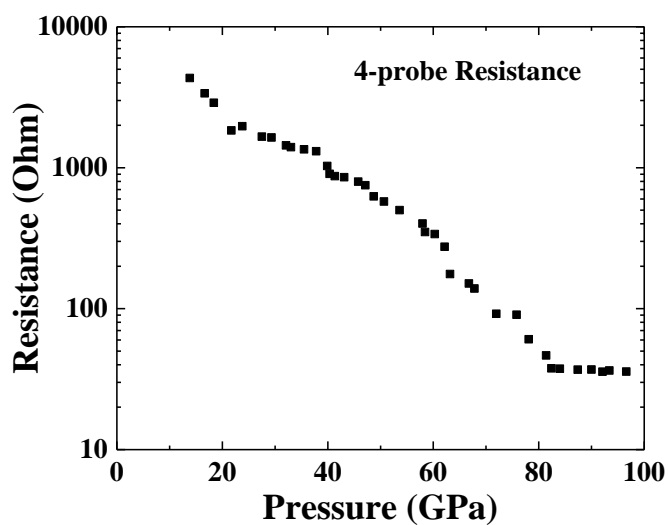


Fig. 3-20 the pressure dependence of electrical resistance at room temperature.

Some typical R-T curves are shown in Fig. 3-21. The resistance shows insulating behavior below 84 GPa, indicating a typical insulator. The negative slopes of the  $dR/dT$  increase with the growing of pressure up to 84 GPa, which reveal that the insulating behavior is suppressed by the increasing of pressure. When the pressure increased to 92 GPa, the insulating behavior was suppressed below 28 K with metallic behavior. This phenomenon that  $dR/dT$  changed from negative to positive is quite similar to the sample in last run at 120 GPa. Considering the appearance of superconductivity with the time lag of 270 days is a long experimental period. Furthermore, the pressure-induced effect also contributes to the superconductivity. In this run, the pressurization of the sample replaces the time annealing effect.

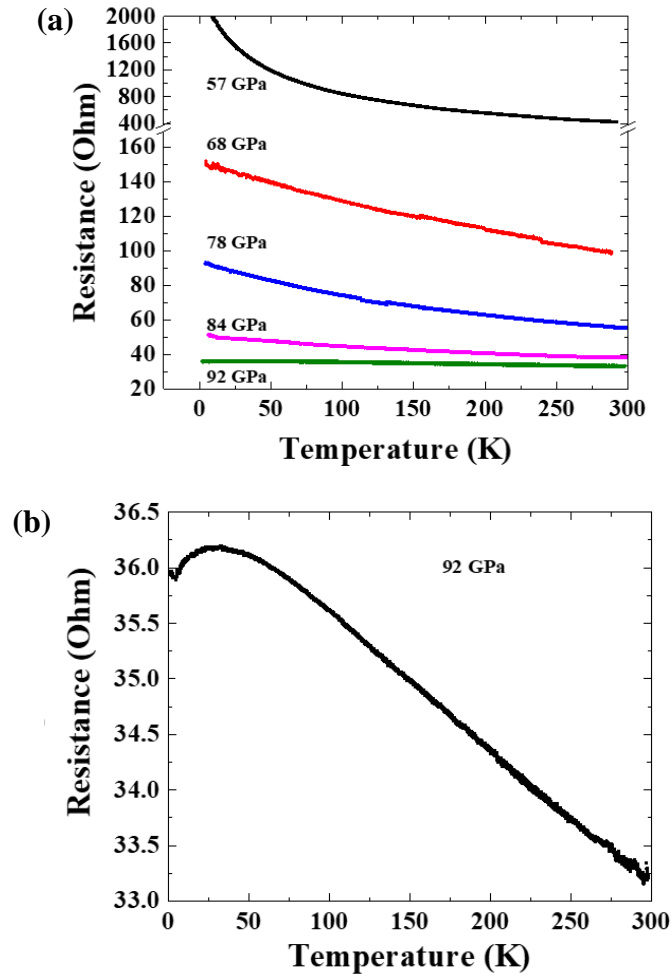


Fig. 3-21 the temperature dependence of resistance from 57 GPa to 92 GPa (a) and the detail at 92 GPa (b).

When the pressure increased to 97 GPa, the sample exhibited insulating behavior at the first cooling cycle. Intriguingly, a drop of resistance at 5 K was observed after 5 days room-temperature annealing in the following cooling cycle as shown in Fig. 3-22. Moreover, it became sharper with the increasing of annealing time at 18 days and 26 days. The drop of the resistance indicated the emergence of the superconducting transition. Compared with the superconducting transition in last run for 270 days, in this case, only 5 days annealing is needed.

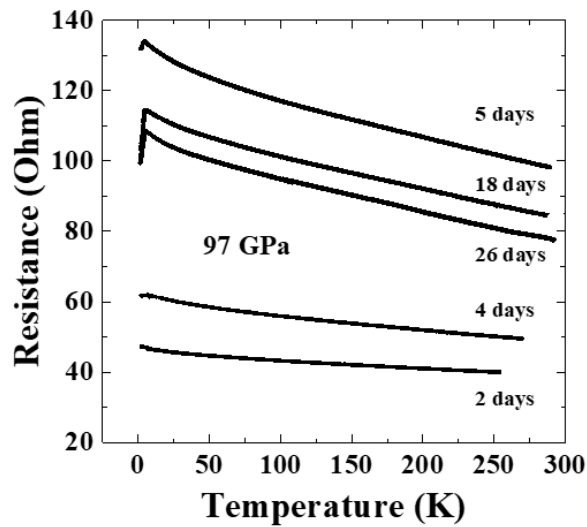


Fig. 3-22 the temperature dependence of resistance at 97 GPa with different annealing days.

With further increasing the pressure, the drop of the resistance behavior retains until 210 GPa the highest pressure of this research. Furthermore, the loss rate of resistance gets more pronounced reaching around 50% and 80% of onset resistance at 102 GPa and 109 GPa as shown in Fig. 3-23. There is no obvious change of temperature dependence of the resistance curve after we check the  $R-T$  relationship at 102 GPa and 109 GPa in various annealing time up to 18 days. It means that the time dependence cannot affect the superconducting phase after the sample shows superconductivity. Meanwhile, from 115 GPa to 210 GPa, the resistance loss rate increases with the growing of the pressure. It means that the pressurization has a position effect on the realization of superconductivity. The increasing of resistance from 109 GPa to 115 GPa derives from the contribution of the

contact resistance between the sample and electrodes in the quasi-four-electrode technique. One of the electrodes broken at 109 GPa, thus a quasi-four-electrode technique was used to check the resistance from 115 GPa. Zero resistance cannot be observed mainly because of the deformation resistance which include the un-superconducting part of the sample in series with the measuring path.

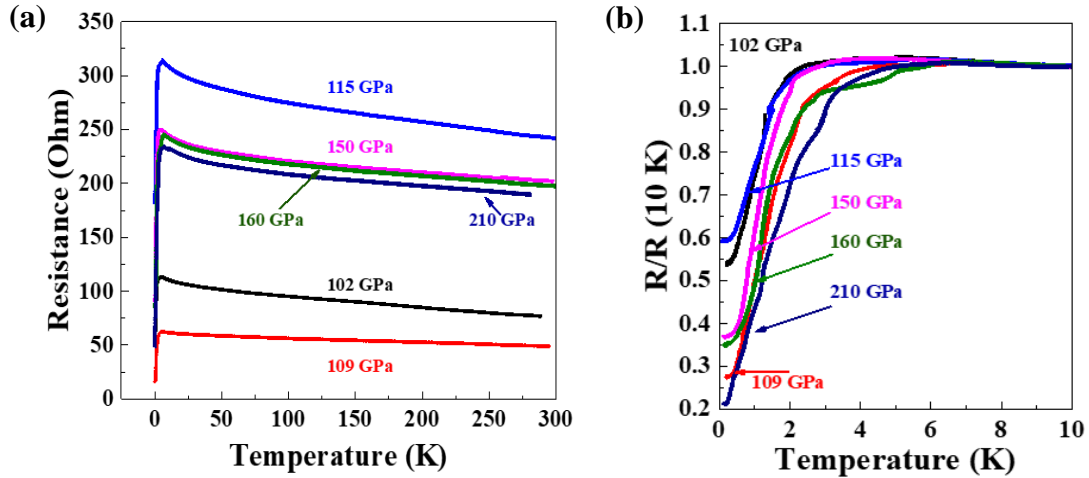


Fig. 3-23 the temperature dependence of resistance at different pressures (a) and the temperature dependence of resistance normalized at 10 K at various pressures.

### 3.3.2 The effect of magnetic field on the temperature dependence of resistance

The observed resistance drop at 97 GPa with 26 days annealing was further examined by the effect of magnetic field on the temperature dependence of resistance as shown in Fig. 3-24. The onset drop of resistance shifts to low temperature direction with the increasing of magnetic field demonstrating the occurrence of natural superconductivity in  $\text{Li}_5\text{MoH}_{11}$ . The occurrence of superconductivity as a function of time shows an effect of the time dependence of resistance phenomenon like the  $\text{BaReH}_9$  shown at 139 GPa, which the superconductivity emerges with the period of time [1].

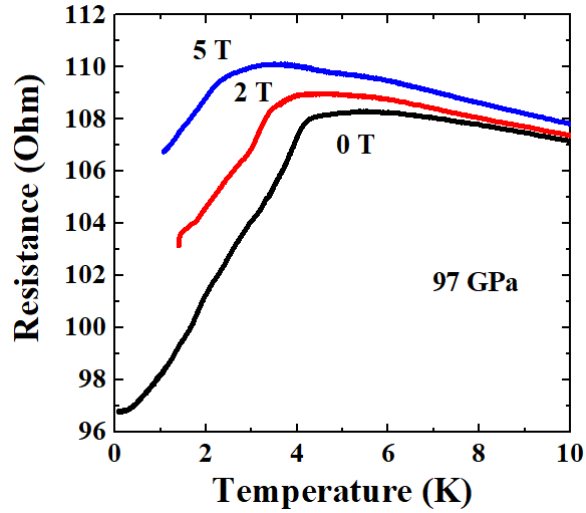


Fig. 3-24 the temperature dependence of resistance at 97 GPa with the effect of various magnetic fields at low temperature region.

It is intriguing that three points of inflection are observed at 160 GPa in the  $R$ - $T$  curve compared with the magnetic field effect at 150 GPa. Moreover, these points were suppressed by the applying of magnetic fields up to 6 T as seen in Fig. 3-25. The results may be explained by the coexistence of three high pressure phases. To further understand this behavior, the relationship between upper critical field and onset transition temperature was plotted in Fig. 3-26. The upper critical field  $H_{c2}$  at zero can be calculated by Werthamer-Helfand-Hohenberg formula  $H_{c2}(0) = -0.693T_c (dH_{c2}/dT)_{T=T_c}$  [6]. The dashed lines represent the temperature dependence of calculated  $H_{c2}$ . The suppress of superconducting transition at 160 GPa is 13.3 T, which is much higher than that of 5.5 T in 150 GPa. J. Ying et al. uncovered a similar changing of the upper critical field with the increasing of pressure due to the phase transition proved by the following Raman measurement [7]. Thus, these results may indicate a possible phase transition at 160 GPa.

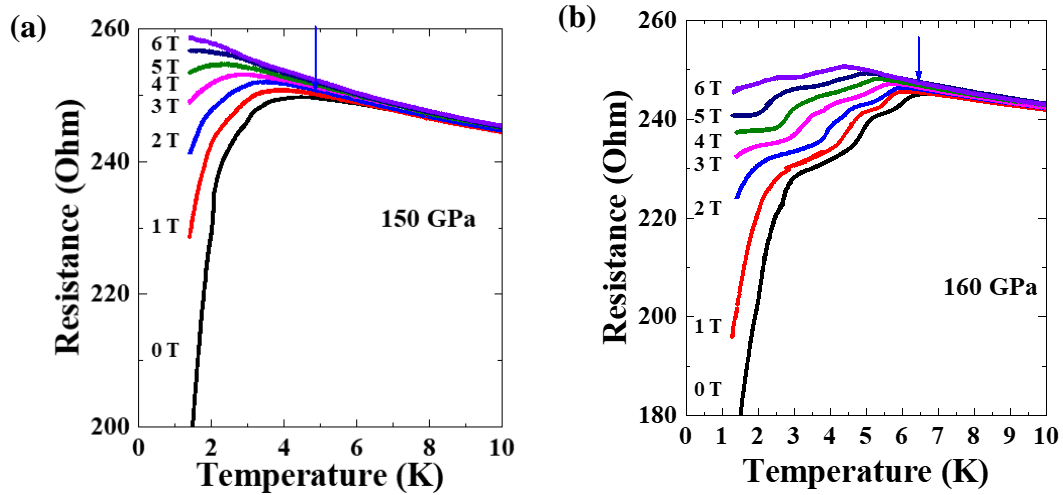


Fig. 3-25 the resistance versus temperature as a function of various magnetic fields at 150 GPa and 160 GPa.

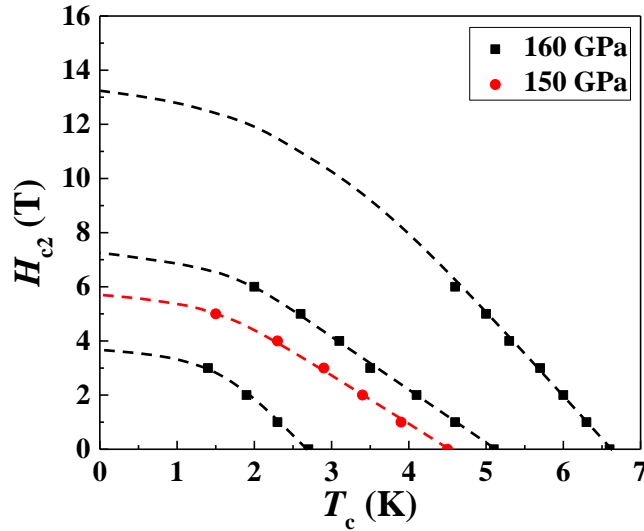


Fig. 3-26 Upper critical field  $H_{c2}$  for the pressure of 150 GPa and 160 GPa, respectively.  $T_c$  was determined from the onset of resistance drop. The dashed lines come from the calculated  $H_{c2}$  based on the Werthamer-Helfand-Hohenberg formula.

### 3.3.3 The diagram of pressure versus temperature

In order to understand the relationship between pressure and  $T_c$ , the pressure dependence of  $T_c$  was plotted in Fig. 3-27. The superconductivity emerged at 97 GPa with

$T_c = 5.4$  K then  $T_c$  gradually decreased to 4.5 K at 155 GPa. At 160 GPa,  $T_c$  rapidly increased to 6.5 K with multi-superconducting phase, at last  $T_c$  maintained 6.5 K to 210 GPa.

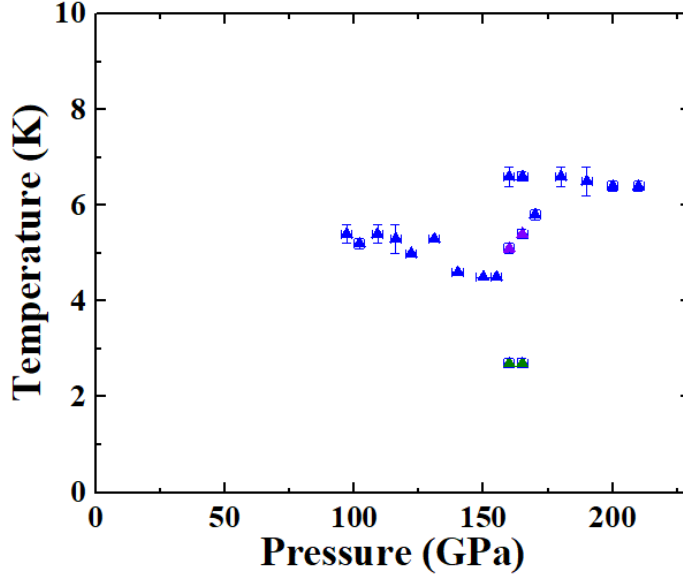


Fig. 3-27 the pressure dependence of  $T_c$  in short time annealing.

### 3.4 The synchrotron powder XRD under high pressure

In order to understand the structural phase transition under the effect of high pressure. The synchrotron powder XRD of the  $\text{Li}_5\text{MoH}_{11}$  was measured under the pressure up to 130 GPa in the DAC with a separate run. Due to the strong peaks of gold in the X-ray pattern, no electrode was chosen in this run. The pressure medium was not used in the XRD measurement and the maximum pressure is 130 GPa due to the broken of diamond. The results point out that  $\text{Li}_5\text{MoH}_{11}$  shows no structural phase transition up to 130 GPa with the ambient pressure hexagonal phase structure as shown in Fig. 3-33. The  $\text{Li}_2\text{O}$  came from the oxidation of the raw material  $\text{LiH}$ . With the increase of pressure, the peaks position shifted to high angle degree and became broaden. Considering the time dependence phenomenon of the sample, the room temperature annealing was conducted at 30GPa for 55 days and 100 GPa for 37 days. The sample kept the hexagonal structure after the room temperature annealing, which indicate no structural phase transition with the time

dependence behavior. The normalized lattice parameters of  $a$ ,  $c$  and volume  $V$  as a function of pressure are shown in Fig. 3-34. A continuous decrease of the lattice parameters with the increase of pressure indicates the shrinkage of the hexagonal structure. The lattice parameters decrease gradually with the increasing of pressure up to 130 GPa where the volume is compressed by 54%.

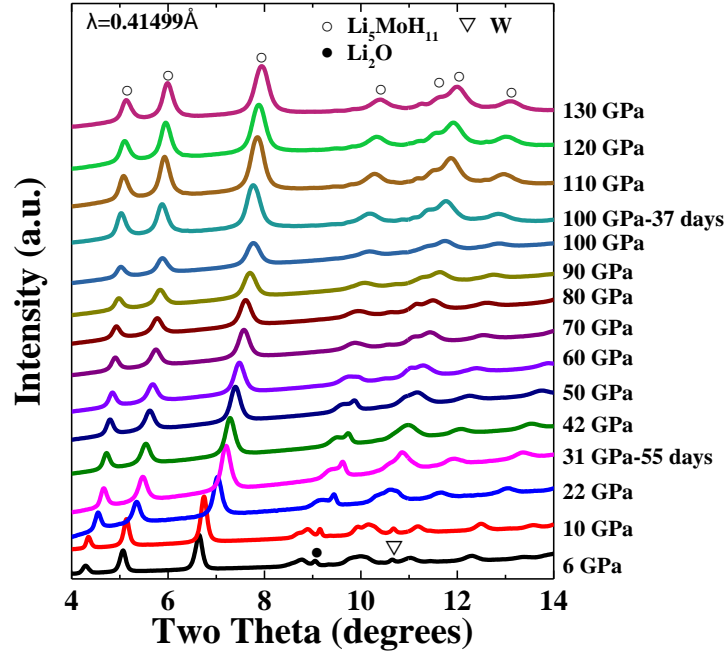


Fig. 3-33 the powder XRD pattern of  $\text{Li}_5\text{MoH}_{11}$  at various pressures up to 130 GPa at room temperature. Open circles indicate the reflection from the  $\text{Li}_5\text{MoH}_{11}$ . The mark of closed circle indicates  $\text{Li}_2\text{O}$ , which is the oxidation product of  $\text{LiH}$ . Open triangle is assignable to tungsten which is the material of needle used for loading sample into DAC.

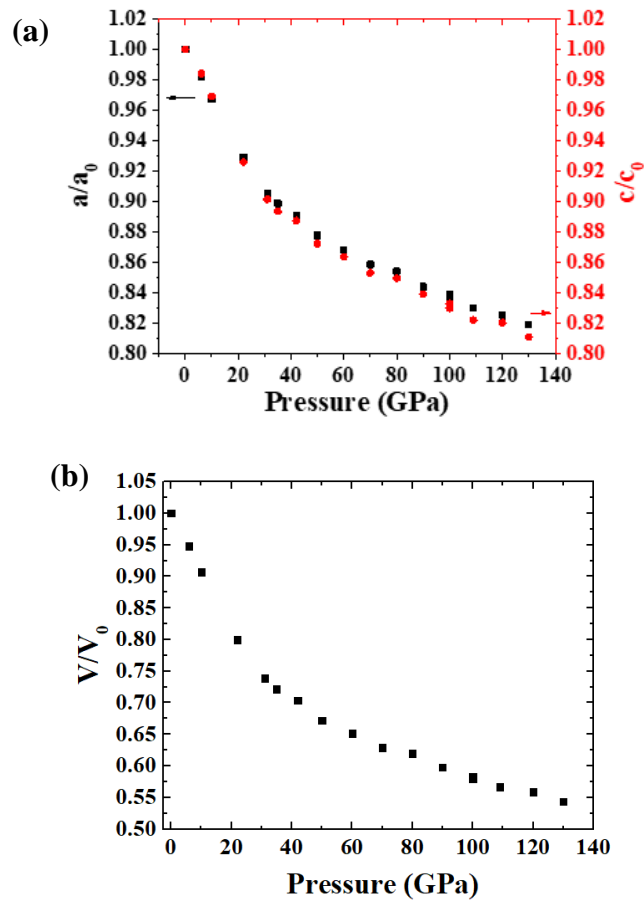


Fig. 3-34 the pressure dependence of the lattice parameters  $a$ ,  $c$  normalized at the ambient pressure (a) and the volume  $V$  normalized at the ambient pressure (b).

## 3.5 Discussion

### 3.5.1 The time dependence behavior

The conducting behavior of  $\text{Li}_5\text{MoH}_{11}$  shows the time dependence behavior. In the long time annealing, the temperature dependence of electrical resistance transformed from insulating behavior to metallic behavior after 48 days room temperature annealing at 77 GPa. The room temperature resistance decreases with the annealing time at 100 GPa, where the slopes of  $dR/dT$  decrease with the annealing time in the  $R$ - $T$  curves. Furthermore, the appearance of the superconducting transition is accompanied with the annealing time.

According to the powder XRD, the sample shows no phase transition up to 130 GPa with the hexagonal  $P6_3cm$  structure even the room temperature annealing was conducted at 30 GPa and 100 GPa, which indicates the mainly structure determined by Li and Mo remains unchanged with the effect of pressure and time. Due to the structure stability, we can deduce that the time dependence behavior is not induced by the phase transition. The possible reason may be the distortion and rotation of the hydrogen cage in the  $\text{MoH}_9$  unit as shown in Fig. 3-35. After the pressure of  $\text{Li}_5\text{MoH}_{11}$  is increased, the  $\text{MoH}_9$  cages are distorted by the high pressure, where the  $\text{MoH}_9$  unit may locate in a metastable state. With the annealing at room temperature, the hydrogen atoms move to a position where the state is relative stable. Thus, the restoring of the distorted  $\text{MoH}_9$  cages lead to this time dependence behavior. The pressure-time path plays an important role in the forming of superconducting phase. Furthermore, based on the calculation of electronic structure of  $\text{Li}_5\text{MoH}_{11}$ , the physical properties of  $\text{Li}_5\text{MoH}_{11}$  are also dominated by the  $\text{MoH}_9$  unit [5]. In the  $\text{BaReH}_9$  case, the restoring of the structural integrity of the highly distorted  $\text{ReH}_9$  prisms leads to the time kinetics effect. It indicates the structure, especially the  $\text{ReH}_9$  cage is in the metastable state. In the recently discovered high  $T_c$  superconductor hydrogen sulfide, the high  $T_c$  phase was observed by the room temperature annealing at 150 GPa. Hence, the annealing process becomes an important role in the exploration of superconductivity under high pressure.

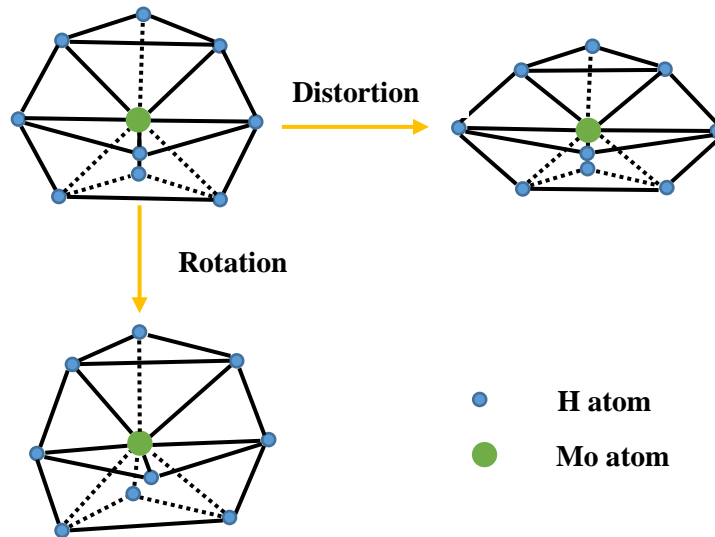


Fig. 3-35 The possible distortion and rotation of hydrogen cages with annealing time.

### 3.5.2 The superconductivity of $\text{Li}_5\text{MoH}_{11}$

The hydrogen-rich metal hydride  $\text{Li}_5\text{MoH}_{11}$  shows superconductivity with the effect of pressure from 100 GPa and retains to 210 GPa. The observed drop of resistance cannot explain by Re gasket because Re shows  $T_c$  of 1.7 K at room temperature and then the  $T_c$  reaches its peak of 3.5 K at 5 GPa, and shows lower than 2 K when the pressure higher than 60 GPa as reported in [8, 9]. The possible decomposition products of Li can exclude by showing semiconducting behavior above 80 GPa [10]. The  $T_c$  of Li can be above 10 K at 30-50 GPa and this is not accordant with the observed result in this experiment [11, 12]. As one of the starting materials of  $\text{Li}_5\text{MoH}_{11}$ , Mo shows the high  $T_c$  at around 1 K [13]. Thus, the superconducting phase can exclude the possibility of Mo. During the making of the gold electrodes on the surface of diamond, the titanium was deposited before the deposition of gold to enhance the bonding strength of gold and diamond due to the better connection of diamond and titanium. Thus, the existence of metal titanium and gold should be considered. The  $T_c$  of Ti shows 2.3 K at 41 GPa and increases to 3.4 K at 56 GPa with the positive effect on pressure [14]. However, in this experiment, no drop of resistance was observed below 60 GPa. Thus we can conclude that the superconductivity does not come from Ti. The pressure dependence of  $T_c$  of the possible elements and  $\text{Li}_5\text{MoH}_{11}$  are plotted in Fig. 3-36. The synchrotron powder XRD results prove that the sample shows no structural phase transition up to 130 GPa. The structure of  $\text{Li}_5\text{MoH}_{11}$  is hexagonal with  $P6_3cm$  at ambient pressure. The mainly structure determined by Li and Mo remains unchanged with the pressure effect. But the possibility of sublattice with the same position of heavy metal cannot be excluded. In  $\text{BaReH}_9$  hydride, the hexagonal structure also keeps no change up to the pressure of 110 GPa. The hexagonal structural stability of the two hydrides both keep to more than 100 GPa. All these above concluded, we can deduce that the superconducting phase is the hexagonal structure  $\text{Li}_5\text{MoH}_{11}$ .

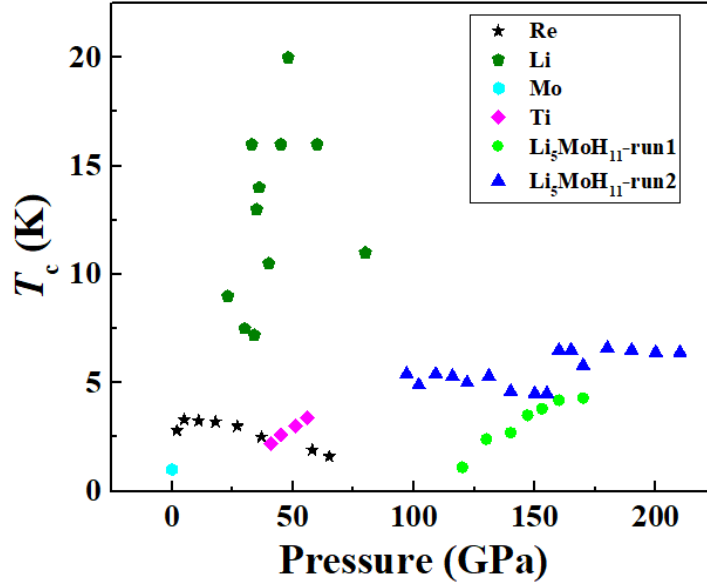


Fig. 3-36 the pressure dependence of  $T_c$  in Re [8, 9], Li [10-12], Mo [13], Ti [14] and  $\text{Li}_5\text{MoH}_{11}$ .

### 3.5.3 The phase diagram of $\text{Li}_5\text{MoH}_{11}$

Since the conducting behavior of  $\text{Li}_5\text{MoH}_{11}$  under high pressure is influenced by the annealing time. Two different annealing time periods were chosen in this experiment. The long time annealing means sufficient time until no change of the resistance and conducting behavior. While the short time annealing is less than half of the long time annealing at similar pressure region. In both case, the metallization and superconductivity were observed.

The phase diagram can be summarized as Fig. 3-37 and Fig. 3-38 with long time annealing and short time annealing, respectively. In both diagram, the insulator to metal transition is observed near 100 GPa. However, the  $T_c$  value is not match well due to the different annealing time periods. In long time annealing case, the superconductivity emerges from 120 GPa with  $T_c$  of 3.0 K and  $T_c$  increases to 4.4 K at 170 GPa. While in short time annealing case, the  $T_c$  appears near 100 GPa with 5.4 K and decreases to 4.5 K at 150 GPa. At 150 GPa, the two runs show similar  $T_c$  value. But, The  $T_c$  rapidly increases to 6.5 K at 160 GPa in short time annealing while keeping stable in long time annealing. The reason may come from the long time annealing effect contributed stable structure. The

time dependence effect may delay the superconducting transformation. Other reasons such as the pressure distribution in the culet of diamond may also lead to the discrepancy of the  $T_c$  value. In the short time annealing case, the multi-superconducting phase was observed at 160-165 GPa and disappeared at 170 GPa. It may indicate the phase transition between 160 and 170 GPa. According to the PXRD, the  $P6_3cm$  phase can keep at least to 130 GPa. Thus, a high-pressure phase may formed above 160 GPa. The coexistence of several superconducting phases may also lead to the mismatch of the phase diagram.

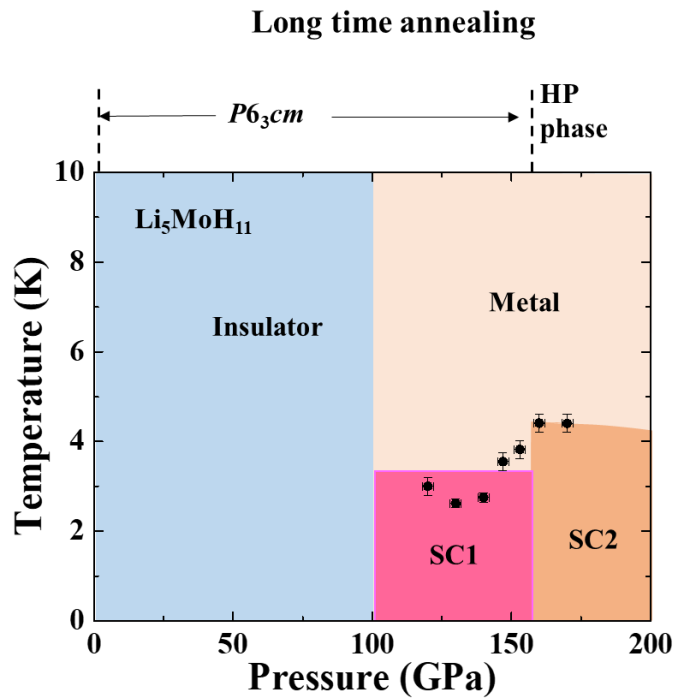


Fig. 3-37 the phase diagram of  $\text{Li}_5\text{MoH}_{11}$  with long time annealing at room temperature.

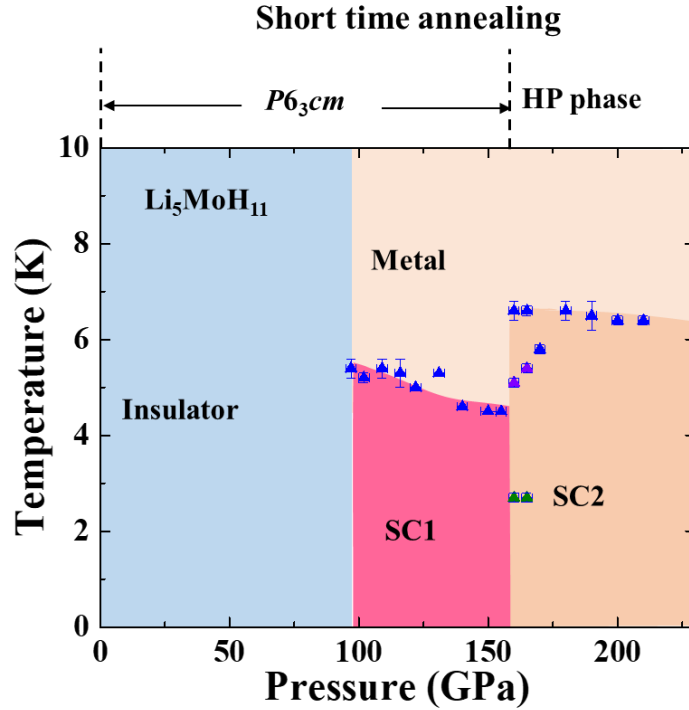


Fig. 3-38 the phase diagram of  $\text{Li}_5\text{MoH}_{11}$  with short time annealing at room temperature.

### 3.5.4 The comparison of $\text{Li}_5\text{MoH}_{11}$ and $\text{BaReH}_9$

Since both  $\text{Li}_5\text{MoH}_{11}$  and  $\text{BaReH}_9$  belong to the transition metal hydrides, they exhibit many similar properties. They are insulators at ambient pressure and show time dependence behavior before the emergence of superconductivity as shown in Fig. 3-39. Furthermore, the appearance of several possible superconducting phases in  $\text{Li}_5\text{MoH}_{11}$  and  $\text{BaReH}_9$  are observed as shown in Fig. 3-40. In  $\text{BaReH}_9$  compound, two inflection points are recognized at 91 GPa. In  $\text{Li}_5\text{MoH}_{11}$  hydride, similar behavior of three points of inflection are confirmed by the applying of magnetic field, which may indicate the phase transition. Besides, these two hydrides all remain their hexagonal structure to high pressure. The value of  $T_c$  and the pressure region of superconducting phase of  $\text{Li}_5\text{MoH}_{11}$  and  $\text{BaReH}_9$  are also quite similar. This similarities may come from the crystal structure belonging to hexagonal structure. Furthermore, the hexagonal structure includes the  $\text{MH}_9$  (M: Re, Mo) unit hybridized by the transition metal and hydrogen atoms. When the discrepancy is considered, we find  $\text{BaReH}_9$  shows a dome shape superconducting phase between 80 GPa and 150 GPa as shown in Fig.

3-41. While the  $T_c$  of  $\text{Li}_5\text{MoH}_{11}$  starts at 97 GPa and remains to 6.5 K from 160 GPa to 210 GPa even a decrease appear to 4.5 K at 155 GPa. A more stable superconducting behavior obtains to more than 200 GPa. Furthermore, considering the effect of laser irradiation on the emergence of superconductivity in  $\text{BaReH}_9$ , we find there is no obvious change of resistance and accelerated superconducting behavior on  $\text{Li}_5\text{MoH}_{11}$  when the laser irradiated to the sample.

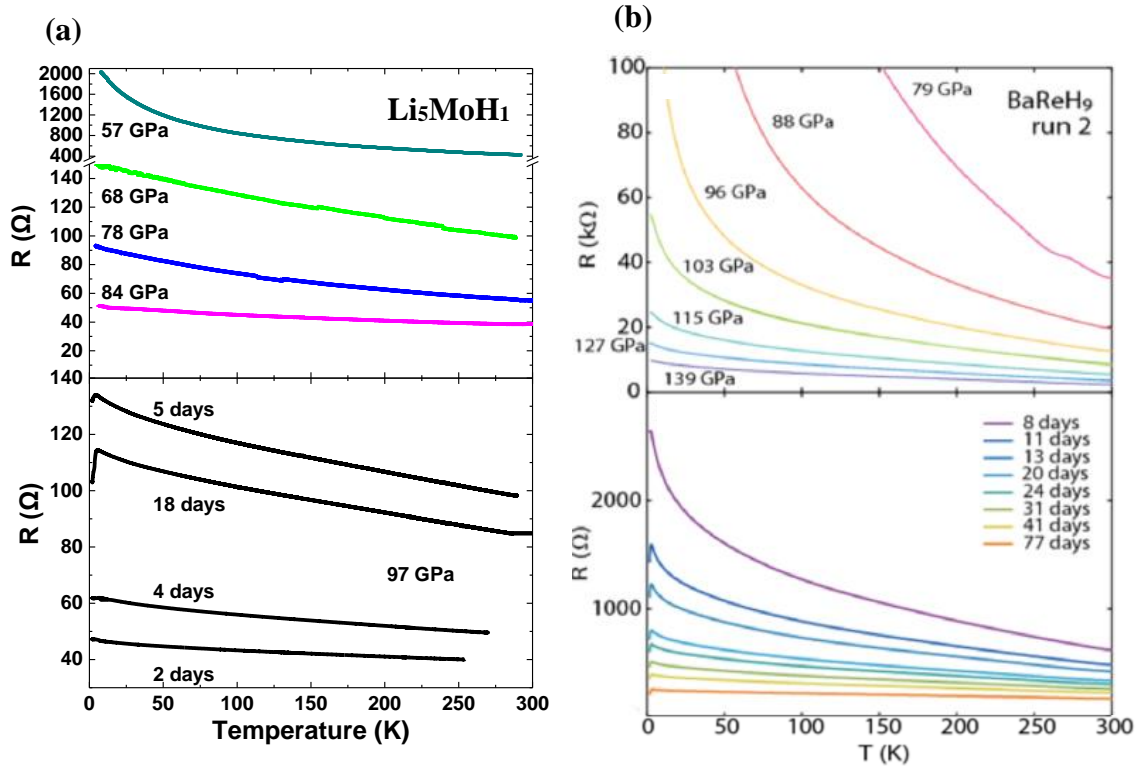


Fig. 3-39 the time dependence behavior of  $\text{Li}_5\text{MoH}_{11}$  (a) and  $\text{BaReH}_9$  (b).

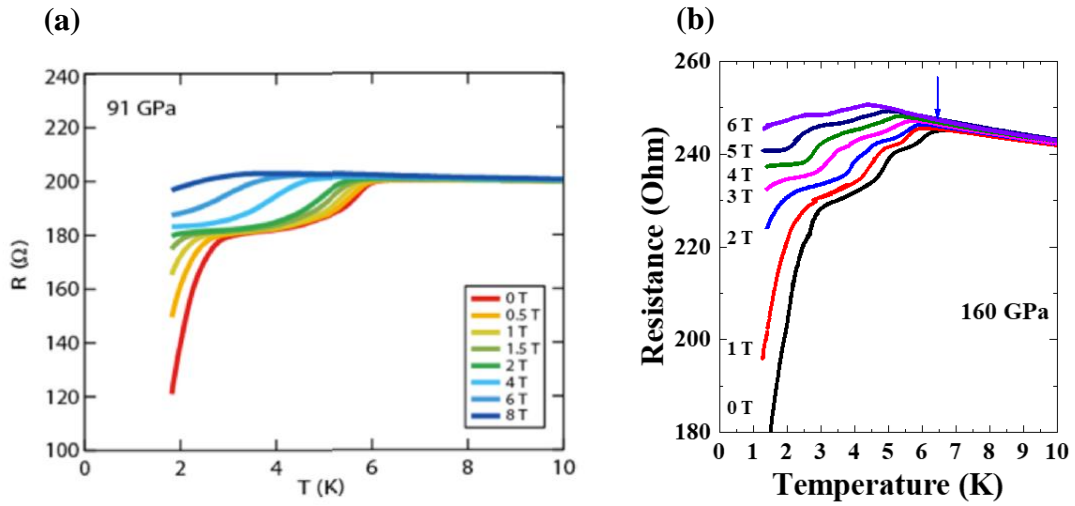


Fig. 3-40 the temperature dependence of resistance with the effect of magnetic field in BaReH<sub>9</sub> (a) and Li<sub>5</sub>MoH<sub>11</sub> (b).

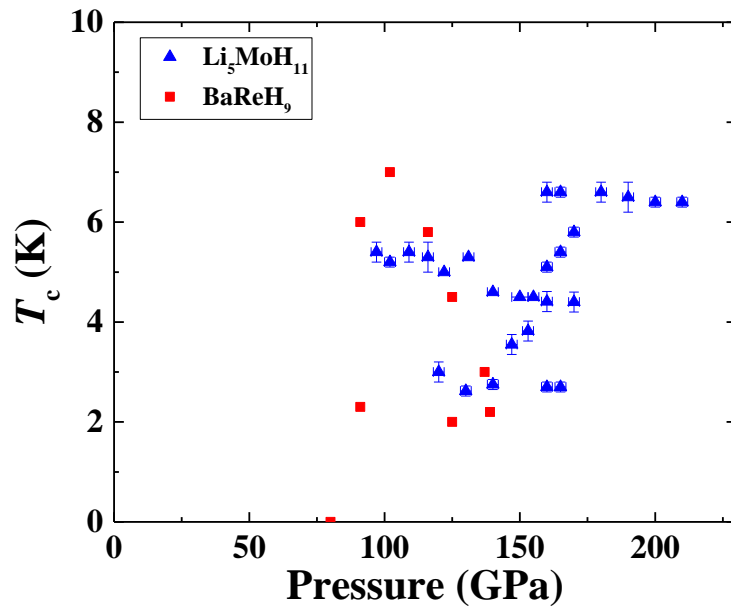


Fig. 3-41 the pressure dependence of  $T_c$  in Li<sub>5</sub>MoH<sub>11</sub> and BaReH<sub>9</sub>.

**Reference:**

- [1] S. Takagi, S. Orimo, Recent progress in hydrogen-rich materials from the perspective of bonding flexibility of hydrogen, *Scr. Mater.* 109 (2015) 1-5.
- [2] S. Takagi, Y. Iijima, T. Sato, H. Saitoh, K. Ikeda, T. Otomo, K. Miwa, T. Ikeshoji, K. Aoki, S. Orimo, True boundary for the formation of homoleptic transition-metal hydride complexes, *Angew. Chem. Int. Ed.* 54 (2015) 5650.
- [3] N.T. Stetson, K. Yvon, P. Fischer, On the structure of the complex hydride BaReH<sub>9</sub>, *Inorg. Chem.* 33 (1994) 4598-4599.
- [4] S. Takagi, Y. Iijima, T. Sato, H. Saitoh, K. Ikeda, T. Otomo, K. Miwa, T. Ikeshoji, S. Orimo, Formation of novel transition metal hydride complexes with ninefold hydrogen coordination, *Sci. Rep.*, 7 (2017) 44253.
- [5] T. Muramatsu, W.K. Wanene, M. Somayazulu, E. Vinitsky, D. Chandra, T.A. Strobel, V. V Struzhkin, R.J. Hemley, Metallization and Superconductivity in the Hydrogen-Rich Ionic Salt BaReH<sub>9</sub>, *J. Phys. Chem. C.*, 119 (2015) 18007-18013.
- [6] N.R. Werthamer, E. Helfand, P.C. Hohenberg, Temperature and purity dependence of the superconducting critical field. *Phys. Rev.*, 147 (1966) 295-302.
- [7] J. Ying, V. V Struzhkin, Z. Cao, A.F. Goncharov, H. Mao, F. Chen, X. Chen, A.G. Gavriliuk, X. Chen, Realization of insulating state and superconductivity in the Rashba semiconductor BiTeCl, *Phys. Rev. B*, 100504 (2016) 1-6.
- [8] C. W. Chu, T. F. Smith, and W. E. Gardner, Superconductivity of Rhenium and Some Rhenium-Osmium Alloys at High Pressure, *Phys. Rev. Lett.*, 20 (1968) 198-201.
- [9] K. Takahama, T. Matsuoka, K. Shimizu. Present at the 13th APS Topical Conference on the Shock Compression of Matter (SHOCK 13), Portland, July 20-25, 2013; Abstract M1.044.
- [10] K. Shimizu, H. Ishikawa, D. Takao, T. Yagi, K. Amaya, Superconductivity in compressed lithium at 20 K, *Nature*, 419 (2002) 597-599.
- [11] T. Matsuoka and K. Shimizu, Direct observation of a pressure-induced metal-to-semiconductor transition in lithium, *Nature*, 458 (2009) 186-189.
- [12] V.V. Struzhkin, M.I. Erements, W. Gan, H.K. Mao, R. Hemley, Superconductivity in dense lithium, *Science*, 298 (2002) 1213-1215.

- [13] J.J. Hamlin, Superconductivity in the metallic elements at high pressures, *Physica C*, 514 (2015) 59-76.
- [14] I.O. Bashkin, V.G. Tissen, M.V. Nefedova, E.G. Ponyatovsky, Superconducting temperature of the  $\omega$ -phase in Ti, Zr and Hf metals at high pressures, *Physica C*, 453 (2007) 12-14.

# Chapter 4. Conclusions

In this thesis, the hydrogen-rich metal hydride  $\text{Li}_5\text{MoH}_{11}$  was investigated through the electrical resistance and synchrotron powder XRD measurements under high pressure and low temperature to explore the possible high  $T_c$  superconductor in the hydrides by the applying of high pressure due to the prediction that chemical pre-compression on hydrides can realize the metallic and superconducting behavior. The following conclusions can be drawn:

The sample is an insulator at ambient pressure and exhibited time dependence behavior. The metallization of the sample is observed at around 100 GPa. The sample shows superconductivity from 100 GPa with the maximum  $T_c$  of 6.5 K at 160 GPa. The superconducting behavior is influenced by the annealing time. The phase diagrams of the sample are summarized according to the annealing time as shown in Fig. 4-1. The  $\text{Li}_5\text{MoH}_{11}$  demonstrates no structural phase transition up to 130 GPa with the hexagonal structure, which claims that the superconducting transition is not derived from the high-pressure by-product but from  $\text{Li}_5\text{MoH}_{11}$ .

These results suggest that apart from the effect of pressure on the changing of conduction and superconductivity, the annealing time treatment can also have an effect on the conducting behavior and superconducting behavior. This work can feedback to the synthesis of high-  $T_c$  metal hydrides.

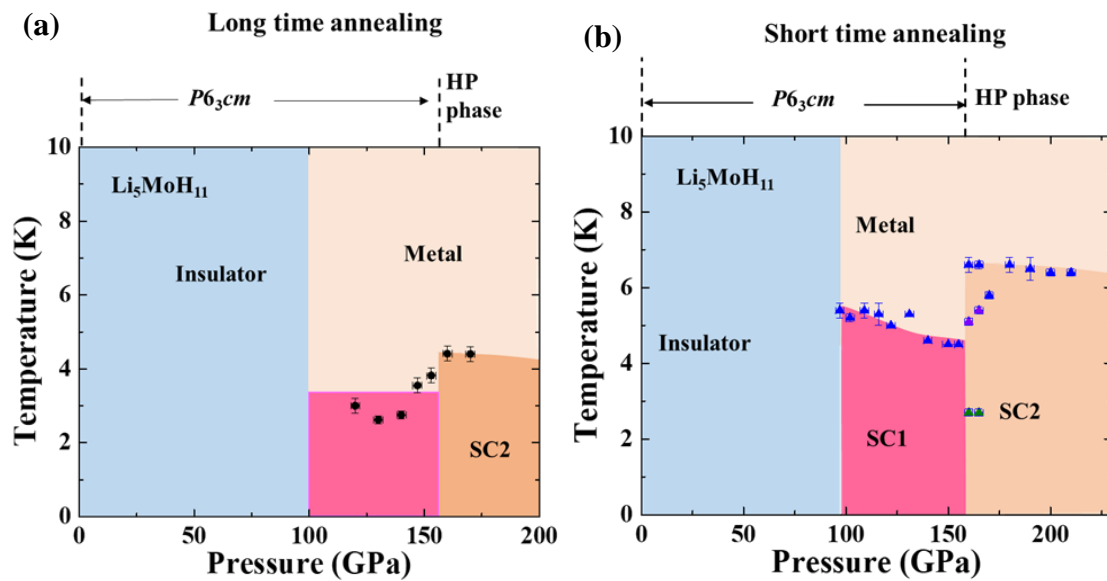


Fig. 4-1 the phase diagram of  $\text{Li}_5\text{MoH}_{11}$  after long time annealing (a) and short time annealing (b).

## Published works

- [1] Resistance measurement of metal hydrides under high pressure. The 17<sup>th</sup> International Conference on High-Pressure in Semiconductor Physics (HPSP-17) and Workshop on High-Pressure Study of Superconductors (WHS), Tokyo, 7-11<sup>th</sup>, Aug., 2016 (Poster).
- [2] Resistance measurement of metal hydride under high pressure. The 4th SKLSHM-KYOKUGEN Workshop on Materials at high pressure, Changchun, 25<sup>th</sup>, Sep., 2016 (Poster).
- [3] Conductive Behavior of Metal Hydride under High Pressure. The 72th Annual meeting of JPS, Osaka, 17-20<sup>th</sup>, Mar., 2017 (Poster).
- [4] Superconductivity of Hydrogen-rich Metal Hydride under High Pressure. The 26th International Conference on High Pressure Science and Technology (AIRAPT 26) Joint with the 8th Asian Conference on High Pressure Research (ACHPR 8) & the 19th China High Pressure Conference (CHPC19), Beijing, 19-23<sup>rd</sup>, Aug., 2017 (Oral).
- [5] Superconductivity of Hydrogen-rich Metal Hydride under High Pressure. The 58<sup>th</sup> High Pressure Conference of Japan, Nagoya, 8-10<sup>th</sup>, Nov. 2017 (Oral).
- [6] Superconductivity of hydrogen-rich metal hydride  $\text{Li}_5\text{MoH}_{11}$  under high pressure, Dezhong Meng, Masafumi Sakata, Katsuya Shimizu, Yuki Iijima, Hiroyuki Saitoh, Toyoto Sato, Shigeyuki Takagi, Shin-ichi Orimo. (Submitted)

# Acknowledgements

I would like to acknowledge many people without whom this dissertation would not be possible.

I would like to thank my supervisor Prof. Katsuya Shimizu for his vectoring, support, encouragement in my three years study. His attentive attitude to the research inspire me deeply. It's his erudition, professionalism and attitude to life infected me so much. I really cherish the time in Shimizu laboratory.

I would like to thank Dr. Masafumi Sakata for the help in the teaching of experimental method and the altruistic devotion in my study. His carefulness and refinement to the experiment make me moved so much. With his help, my life becomes much easier in Japan.

I would like to thank Dr. Tomoko Kagayama for her suggestion and help in my experiment, Dr. Yuki Nakamoto for her kindness, encouragement and help in experiment, Dr. Yoshimi Mita for his help in the Raman experiment, Dr. Mari Einaga for her encouragement and help in XRD experiment, Dr. Takahiro Ishikawa and Dr. Akitaka Nakanishi for their help in the theory of high pressure knowledge, Dr. Prasad Gayan Hettiarachchi for his help in improving my English, Dr. Huyen Nguyen for the help in experiment, Ms. Aki Tsukagoshi for her kindness and help in my research, Mr. Makino for his positive attitude in lab.

I would like to thank the students in Shimizu Laboratory for their help in my research and daily life. They always kindly help me to transfer and carry the helium, explain the experimental detail to me, in translation and daily life. Especially for Mr. Hidenori Fujita, he is always sacrificing his time in helping my experiment.

I would like to thank Dr. Yuki Iijima, Dr. Toyoto Sato, Dr. Shigeyuki Takagi, Dr. Shin-ichi Orimo from Tohoku University and Dr. Hiroyuki Saitoh from National Institutes for Quantum and Radiological Science and Technology for their help in the preparation of the samples.

I would like to thank the office staffs in the Graduate School of Engineering Science, Ms. Hanako Nakajima, Mr. Toshinori Kato for their help in the office work before and after I study in Osaka University, the Advisement Office for International Students in

Graduate School of Engineering Science, Ms. Emiko Tasaka for her kindness and help in my life in Japan.

I would like to thank Prof. Wen Yue from China University of Geosciences (Beijing) for his encouragement and support.

I would like to thank my parents for their great support and encouragement.

I would like to thank my girlfriend Zhiyu Li for her accompany, encouragement and help in my daily life.

I would like to thank the China Scholarship Council (CSC) for the financial support during the three years in Osaka University.